

Production of charged pions, kaons, and (anti-)protons in Pb-Pb and inelastic pp collisions at $\sqrt{s_{NN}} = 5.02$ TeV

S. Acharya *et al.**
(ALICE Collaboration)

 (Received 14 November 2019; accepted 2 March 2020; published 29 April 2020)

Midrapidity production of π^\pm , K^\pm , and $(\bar{p})p$ measured by the ALICE experiment at the CERN Large Hadron Collider, in Pb-Pb and inelastic pp collisions at $\sqrt{s_{NN}} = 5.02$ TeV, is presented. The invariant yields are measured over a wide transverse momentum (p_T) range from hundreds of MeV/ c up to 20 GeV/ c . The results in Pb-Pb collisions are presented as a function of the collision centrality, in the range 0–90%. The comparison of the p_T -integrated particle ratios, i.e., proton-to-pion (p/π) and kaon-to-pion (K/π) ratios, with similar measurements in Pb-Pb collisions at $\sqrt{s_{NN}} = 2.76$ TeV show no significant energy dependence. Blast-wave fits of the p_T spectra indicate that in the most central collisions radial flow is slightly larger at 5.02 TeV with respect to 2.76 TeV. Particle ratios (p/π , K/π) as a function of p_T show pronounced maxima at $p_T \approx 3$ GeV/ c in central Pb-Pb collisions. At high p_T , particle ratios at 5.02 TeV are similar to those measured in pp collisions at the same energy and in Pb-Pb collisions at $\sqrt{s_{NN}} = 2.76$ TeV. Using the pp reference spectra measured at the same collision energy of 5.02 TeV, the nuclear modification factors for the different particle species are derived. Within uncertainties, the nuclear modification factor is particle species independent for high p_T and compatible with measurements at $\sqrt{s_{NN}} = 2.76$ TeV. The results are compared to state-of-the-art model calculations, which are found to describe the observed trends satisfactorily.

DOI: [10.1103/PhysRevC.101.044907](https://doi.org/10.1103/PhysRevC.101.044907)

I. INTRODUCTION

Previous observations at the Relativistic Heavy-Ion Collider (RHIC) and at the CERN Large Hadron Collider (LHC) demonstrated that in high-energy heavy-ion (A - A) collisions, a strongly interacting quark-gluon plasma (sQGP) [1–5] is formed. It behaves as a strongly coupled near-perfect liquid with a small viscosity-to-entropy ratio η/s [6]. The experimental results have led to the development and adoption of a standard theoretical framework for describing the bulk properties of the QGP in these collisions [7]. In this paradigm, the beam energy dependence is mainly encoded in the initial energy density (temperature) of the QGP. After formation, the QGP expands hydrodynamically as a near perfect liquid before it undergoes a chemical freeze-out. The chemical freeze-out temperature is nearly beam-energy independent for center-of-mass energy per nucleon pair larger than 10 GeV [7,8]. The hadronic system continues to interact (elastically) until kinetic freeze-out. We report in this paper a comprehensive study of bulk particle production at the highest beam energy for A - A collisions available at the LHC. We probe the highest

QGP temperature, to further study this paradigm and address its open questions.

Transverse momentum distributions of identified particles in Pb-Pb collisions provide information on the transverse expansion of the QGP and the freeze-out properties of the ensuing hadronic phase. By analyzing the p_T -integrated yields in Pb-Pb collisions it has been shown that hadron yields in high-energy nuclear interactions can be described assuming their production at thermal and chemical equilibrium [9–12], with a single chemical freeze-out temperature, $T_{\text{ch}} \approx 156$ MeV, close to the one predicted by lattice QCD calculations for the QGP-hadronic phase transition, $T_c = (154 \pm 9)$ MeV [13]. Indeed, the Pb-Pb data from LHC Run 1 [14] showed an excellent agreement with the statistical hadronization model with the exception of the proton and antiproton, $(\bar{K}^*)K^*$ and multistrange particle yields [9,12]. The deviation could be in part due to interactions in the hadronic phase, which result in baryon-antibaryon annihilation that is most significant for (anti-)protons [15–18]. Proposed explanations for the observed discrepancy with respect to the thermal model predictions can be found in Refs. [18–22]. Moreover, at $\sqrt{s_{NN}} = 2.76$ TeV the proton-to-pion [$(p + \bar{p})/(\pi^+ + \pi^-) \equiv p/\pi$] ratio exhibits a slight decrease with centrality and a slightly lower value than measured at RHIC. New measurements at $\sqrt{s_{NN}} = 5.02$ TeV, which exploit the currently highest medium density, could provide an improved understanding of the particle production mechanisms [22].

The spectral shapes at low p_T ($p_T < 2$ GeV/ c) in central Pb-Pb collisions at $\sqrt{s_{NN}} = 2.76$ TeV showed a stronger radial

*Full author list given at the end of the article.

Published by the American Physical Society under the terms of the [Creative Commons Attribution 4.0 International](https://creativecommons.org/licenses/by/4.0/) license. Further distribution of this work must maintain attribution to the author(s) and the published article's title, journal citation, and DOI.

flow than that measured at RHIC energies, in agreement with the expectation based on hydrodynamic models [14,23]. The results for identified particle production at low p_T and higher $\sqrt{s_{NN}}$ are useful to further test hydrodynamic predictions.

At intermediate p_T ($2 - 10$ GeV/ c), the particle ratios experimentally show the largest variation and in particular for the baryon-to-meson enhancement several new hadronization mechanisms have been proposed [24–26]. In the most central Pb-Pb collisions at $\sqrt{s_{NN}} = 2.76$ TeV, the p/π ratio reaches values larger than 0.8 for $p_T \approx 3$ GeV/ c , which surpass those for inelastic pp collisions at the same energy [27,28]. An intermediate p_T enhancement of heavier hadrons over lighter hadrons is expected from the collective hydrodynamic expansion of the system alone [29–31]. In coalescence models [32–34], which requires radial flow as well, baryon-to-meson ratios are further enhanced at intermediate p_T by the coalescence of lower p_T quarks that leads to a production of baryons (3 quarks) with larger p_T than for mesons (2 quarks). The baryon-to-meson ratio decreases at high p_T and reaches the values observed in pp collisions as a consequence of the increasing importance of parton fragmentation. The observation of a qualitatively similar enhancement of the kaon-to-pion $[(K^+ + K^-)/(\pi^+ + \pi^-) \equiv K/\pi]$ ratio in central Pb-Pb collisions with respect to inelastic pp collisions [28,35] supports an interpretation based on the collective radial expansion of the system that affects heavier particles more.

For high p_T ($p_T > 10$ GeV/ c), measurements of the production of identified particles in Pb-Pb collisions relative to inelastic pp collisions contribute to the study of hard probes propagating through the medium. This offers the possibility to determine the properties of the QGP like the transport coefficient \hat{q} [36] and the space-time profile of the bulk medium in terms of local temperature and fluid velocity [37]. The modification of particle production is quantified with the nuclear modification factor, R_{AA} , defined as

$$R_{AA} = \frac{d^2N^{AA}/(dydp_T)}{\langle T_{AA} \rangle d^2\sigma^{pp}/(dydp_T)}, \quad (1)$$

where $d^2N^{AA}/(dydp_T)$ is the particle yield in nucleus-nucleus collisions and σ^{pp} is the production cross section in pp collisions. The average nuclear overlap function is represented by $\langle T_{AA} \rangle$ and is obtained from a Glauber model calculation [38]. It is related to the average number of binary nucleon-nucleon collisions $\langle N_{coll} \rangle$, and the total inelastic nucleon-nucleon cross section, $\sigma_{INEL}^{NN} = (67.6 \pm 0.6)$ mb at $\sqrt{s_{NN}} = 5.02$ TeV [39], as $\langle T_{AA} \rangle = \langle N_{coll} \rangle / \sigma_{INEL}^{NN}$. Several measurements of R_{AA} at high p_T for different $\sqrt{s_{NN}}$ [40–46] support the formation of a dense partonic medium in heavy-ion collisions where hard partons lose energy via a combination of elastic and inelastic collisions with the constituents of the QGP [47]. Results from Pb-Pb collisions at $\sqrt{s_{NN}} = 2.76$ TeV showed that within uncertainties, the suppression is the same for pions, kaons and (anti-)protons [28]. Moreover, the inclusive charged-particle nuclear modification factor measured in Pb-Pb collisions at 5.02 TeV shows that the suppression continues to diminish for p_T above 100 GeV/ c [48] while the suppression of jets saturates at a value of 0.5 [49]. Particle production at high transverse momentum has also been studied as a function of the Bjorken energy density [50] and path length [51–53].

The results show interesting scaling properties which can be further tested using LHC data at higher energies.

In this paper, the measurement of p_T spectra of π^\pm , K^\pm and $(\bar{p})p$ in inelastic pp and Pb-Pb collisions at $\sqrt{s_{NN}} = 5.02$ TeV over a wide p_T range, from 100 MeV/ c for pions, 200 MeV/ c for kaons, and 300 MeV/ c for (anti-)protons, up to 20 GeV/ c for all species, are presented. Particles are identified by combining several particle identification (PID) techniques based on specific ionization energy loss (dE/dx) and time-of-flight measurements, Cherenkov radiation detection and the identification of the weak decays of charged kaons via their kink-topology. The article is organized as follows: Sec. II outlines the analysis details including the track and event selections as well as the particle identification strategies. The obtained results are discussed in Sec. III. Section IV presents the comparison of data with model predictions. Finally, Sec. V contains a summary of the main results.

II. DATA ANALYSIS

In this paper the measurements obtained with the central barrel of the ALICE detector, which has full azimuthal coverage around midrapidity, $|\eta| < 0.8$ [54], are presented. A detailed description of the ALICE detector can be found in Ref. [55].

The pp results were obtained from the analysis of $\approx 1.2 \times 10^8$ minimum bias pp collisions, collected in 2015. The Pb-Pb analysis with ITS and TOF uses $\approx 5 \times 10^6$ minimum bias Pb-Pb collisions, collected in 2015. The Pb-Pb analysis where PID is provided by the TPC, the high momentum particle identification (HMPID) detector and the kink decay topology requires more statistics and uses the full data sample collected in 2015 corresponding to $\approx 6.5 \times 10^7$ Pb-Pb collisions.

Both in pp and Pb-Pb collisions, the interaction trigger is provided by a pair of forward scintillator hodoscopes, the V0 detectors, which cover the pseudorapidity ranges $2.8 < \eta < 5.1$ (V0A) and $-3.7 < \eta < -1.7$ (V0C) [56]. The minimum bias trigger is defined as a coincidence between the V0A and the V0C trigger signals. The V0 detector signals, which are proportional to the charged-particle multiplicities, are used to divide the Pb-Pb event sample into centrality classes, defined in terms of percentiles of the hadronic cross section [38]. A Glauber Monte Carlo model is fitted to the V0 amplitude distribution to compute the fraction of the hadronic cross section corresponding to any given range of V0 amplitudes. The 90–100% centrality class has substantial contributions from QED processes ($\approx 20\%$) [38] and its low track multiplicity presents difficulties in the extraction of the trigger inefficiency; it is therefore not included in the results presented here. Also, an offline event selection is used to remove beam background events. It employs the information from two zero degree calorimeters (ZDCs) positioned at 112.5 m on either side of the nominal interaction point. Beam background events are removed by using the V0 timing information and the correlation between the sum and the difference of times measured in each of the ZDCs [55].

The central barrel detectors are located inside a solenoidal magnet providing a magnetic field of 0.5 T and are used

for tracking and particle identification. The innermost barrel detector is the inner tracking system (ITS) [57], which consists of six layers of silicon devices grouped in three detector systems (from the innermost outwards): the silicon pixel detector (SPD), the silicon drift detector (SDD), and the silicon strip detector (SSD). The time projection chamber (TPC), the main central-barrel tracking device, follows outwards. The results are presented for primary particles, defined as particles with a mean proper lifetime $\tau > 1$ cm/c which are either produced directly in the interaction or from decays of particles with $\tau < 1$ cm/c, restricted to decay chains leading to the interaction [58]. To limit the contamination due to secondary particles and tracks with wrongly associated hits and to ensure high tracking efficiency, tracks are required to cross at least 70 TPC readout rows with a χ^2 normalized to the number of TPC space-points (“clusters”), χ^2/NDF , lower than 2. Tracks are also required to have at least two hits reconstructed in the ITS out of which at least one is in the SPD layers and to have a distance of closest approach (DCA) to the interaction vertex in the direction parallel to the beam axis (z), $|\text{DCA}_z| < 2$ cm. A p_T -dependent selection on the DCA in the transverse plane (DCA_{xy}) of the selected tracks to the primary vertex is also applied [59]. Furthermore, the tracks associated with the decay products of weakly decaying kaons (“kinks”) are rejected. The latter selection is not applied in the study of kaon production from kink decay topology. The primary vertex position is determined from tracks, including short track segments reconstructed in the SPD [60]. The position of the primary vertex along the beam axis is required to be within 10 cm from the nominal interaction point. The position along z of the SPD and track vertices are required to be compatible within 0.5 cm. This ensures a uniform acceptance and reconstruction efficiency in the pseudorapidity region $|\eta| < 0.8$ and rejects pileup events in pp collisions. Different PID detectors are used for the identification of the different particle species. Ordering by p_T , from lowest to highest, the results are obtained using the dE/dx measured in the ITS and the TPC [61], the time of flight measured in the time-of-flight (TOF) detector [62], the Cherenkov angle measured in the high-momentum particle identification detector (HMPID) [63] and the TPC dE/dx in the relativistic rise region of the Bethe-Bloch curve. The performance of these devices is reported in Ref. [55].

A. Particle identification strategy

For the analysis presented here, pions, kaons, and (anti-)protons have been identified following the same analysis techniques as in the previous ALICE measurements. The ITS, TPC (low p_T) and TOF analyses are described in Refs. [14,64,65], while the HMPID and TPC (high p_T) analyses are documented in Refs. [28,35,66]. The kink analysis is described in Ref. [59]. In this paper, only the most relevant aspects of each specific analysis are described.

In most analyses, the yield is extracted from the number-of-sigma (N_σ) distribution. This quantity is defined as

$$N_\sigma^i = \frac{(\text{signal} - \langle \text{signal} \rangle_i)}{\sigma_i}, \quad (2)$$

where i refers to a given particle species ($i = \pi, K, p$), signal is the detector PID signal (e.g., dE/dx), and $\langle \text{signal} \rangle_i$ and σ_i are the expected average PID signals in a specific detector and its standard deviation, respectively.

Figure 1 shows the pion-kaon and kaon-proton separation power as a function of p_T for ITS, TPC, TOF, and HMPID. The separation power is defined as follows:

$$\begin{aligned} \text{Sep}_{(\pi,K)} &= \frac{\Delta_{\pi,K}}{\sigma_\pi} = \frac{|\langle \text{signal} \rangle_\pi - \langle \text{signal} \rangle_K|}{\sigma_\pi}; \\ \text{Sep}_{(K,p)} &= \frac{\Delta_{K,p}}{\sigma_K} = \frac{|\langle \text{signal} \rangle_K - \langle \text{signal} \rangle_p|}{\sigma_K}. \end{aligned} \quad (3)$$

Note that the response for the individual detectors is momentum (p) dependent. However, since results are reported in transverse momentum bins, the separation power as a function of p_T has been evaluated, averaging the momentum-dependent response over the pseudorapidity range $|\eta| < 0.5$. In Table I the transverse momentum ranges covered with each PID technique in the analysis are reported for pions, kaons and (anti-)protons.

a. ITS analysis. The four outer layers of the ITS provide specific energy-loss measurements. The dynamic range of the analog readout of the detector is large enough [67] to provide dE/dx measurements for highly ionizing particles. Therefore, the ITS can be used as a standalone low- p_T PID detector in the nonrelativistic region where the dE/dx is proportional to $1/\beta^2$. For each track, the energy loss fluctuation effects are reduced by using a truncated mean: the average of the lowest two dE/dx values in case four values are measured, or a weighted sum of the lowest (weight 1) and the second lowest (weight 1/2), in case only three values are available.

The plane ($p; dE/dx$) is divided into identification regions where each point is assigned a unique particle identity. The identity of a track is assigned based on which dE/dx curve the track is closest to, removing in this way the sensitivity to the dE/dx resolution. To reject electrons, a selection on $|N_\sigma^\pi| < 2$, is applied.

Using this strategy, it is possible to identify π and K with an efficiency of about 96–97% above $p_T = 0.3$ GeV/c, and $(\bar{p})p$ with an efficiency of 91–95% in the entire p_T range of interest. In the lowest p_T bin, the PID efficiency reaches $\approx 60\%$, $\approx 80\%$, and $\approx 91\%$ for pions, kaons, and (anti-)protons, respectively. By means of this technique it is possible to identify π^\pm , K^\pm , and $(\bar{p})p$ in Pb-Pb (pp) collisions in the p_T ranges 0.1–0.7 GeV/c, 0.2–0.5 (0.6) GeV/c, and 0.3–0.6 (0.65) GeV/c, respectively.

b. TOF analysis. The analysis with the TOF detector uses the subsample of tracks for which a time measurement with TOF is available. The time of flight t_{TOF} is the difference between the measured particle arrival time τ_{TOF} and the event time t_0 , namely $t_{\text{TOF}} = \tau_{\text{TOF}} - t_0$. In the ALICE experiment, the t_0 value can be obtained with different techniques [68]. The best precision on the t_0 evaluation is obtained by using the TOF detector itself. In this case, the t_0 is obtained on an event-by-event basis by using a combinatorial algorithm that compares the measured τ_{TOF} with the expected one under different mass hypotheses. The procedure to evaluate t_0 with the TOF detector is fully efficient if enough reconstructed

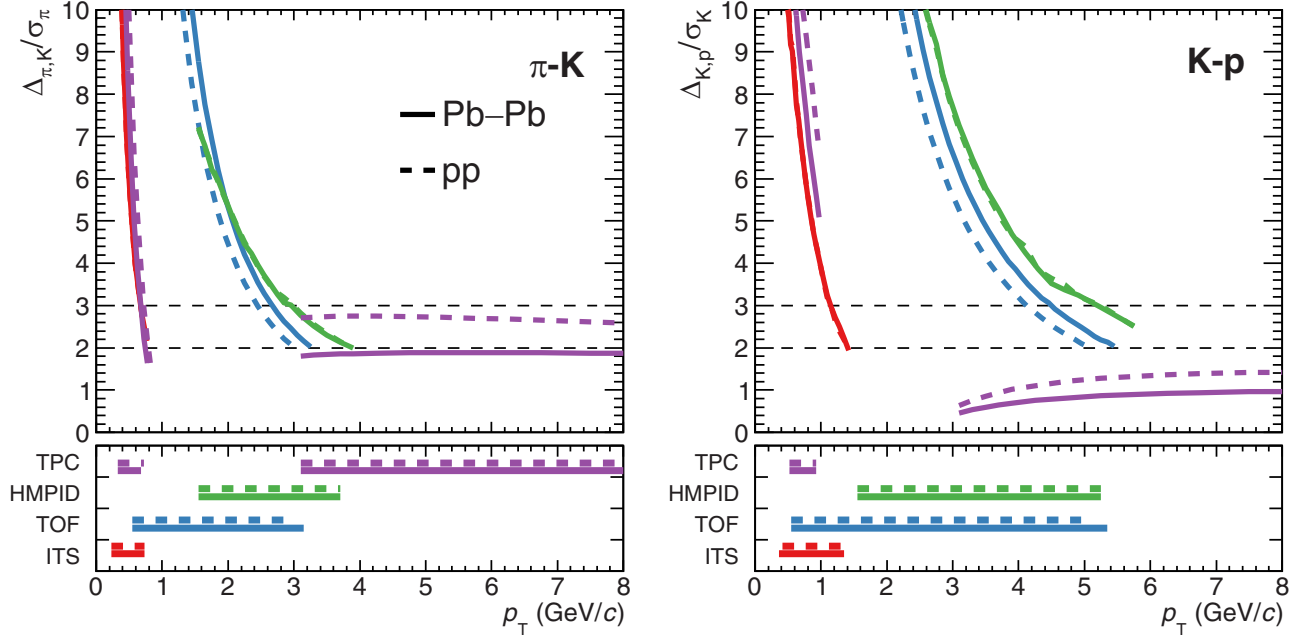


FIG. 1. Separation power of hadron identification in the ITS (red), TPC (magenta), TOF (blue), and HMPID (green) as a function of p_T at midrapidity for inelastic pp and 0–90% Pb-Pb collisions at $\sqrt{s_{NN}} = 5.02$ TeV. The left (right) panel shows the separation of pions and kaons (kaons and protons), expressed as the distance between the expected average PID signal divided by the resolution for the pion (kaon) [see Eq. (3)], averaged over $|\eta| < 0.5$. The lower panels show the range in which the ITS, TPC, TOF, and HMPID provide a separation power $\approx 2\sigma$ or larger.

tracks are available, which is the case of the 0–80% Pb-Pb collisions. The resolution on the t_0 evaluated with the TOF detector is better than 20 ps if more than 50 tracks are used for its determination. This improvement with respect to Run 1 performance [68] is due to improved calibration procedures carried out during Run 2. Overall the TOF signal resolution is about 60 ps in central Pb-Pb collisions. In pp and 80–90% Pb-Pb collisions the measurement of the event time relies on the T0 detector ($\sigma_{t_0} \approx 50$ ps) [68] or, in case it is not available, on the bunch crossing time, which has the worst resolution (≈ 200 ps). The PID procedure is based on a statistical unfolding of the time-of-flight N_σ distribution. For each p_T bin, the expected shapes for π^\pm , K^\pm , and $(\bar{p})p$ are fitted to the t_{TOF} distributions, allowing the three particles to be distinguished when the separation is as low as $\approx 2\sigma$. An additional template is needed to account for the tracks that are wrongly associated with a hit in the TOF. The templates are built from data as described in Ref. [14]. For this purpose

TABLE I. Transverse momentum ranges (in GeV/c) and the corresponding PID methods for pions, kaons, and (anti-)protons. Values in parenthesis refer to pp analysis.

Technique	π^\pm (GeV/c)	K^\pm (GeV/c)	p and \bar{p} (GeV/c)
ITS	0.1–0.7	0.2–0.5(0.6)	0.3–0.6 (0.65)
TPC (low p_T)	0.25–0.7	0.25–0.45	0.4–0.8
TPC (high p_T)	3.0–20.0	4.0–20.0	4.0–20.0
TOF	0.6–3.5	1.00 (0.65)–3.5	0.8–4.5
HMPID	1.5–4.0	1.50–4.0	1.5–6.0
Kinks	–	0.5–6.0 (4.0)	–

the length of measured tracks is used to compute a realistic distribution of the expected time of arrival for each mass hypothesis and the signal shape is reproduced by sampling the parametrized TOF response function (described by a Gaussian with an exponential tail) obtained from data. Since the rapidity of a track depends on the particle mass, the fit is repeated for each mass hypothesis. TOF analysis makes identification of π^\pm , K^\pm , and $(\bar{p})p$ in Pb-Pb (pp) collisions possible in the p_T ranges 0.60–3.50 GeV/c, 1.00 (0.65)–3.50 GeV/c and 0.80–4.50 GeV/c, respectively.

c. TPC analysis. The TPC provides information for particle identification over a wide momentum range via the specific energy loss [55]. Up to 159 space-points per trajectory can be measured. A truncated mean, utilizing 60% of the available clusters, is employed in the dE/dx determination [61]. The dE/dx resolution for the Minimum Ionizing Particle (MIP) is $\approx 5.5\%$ in peripheral and $\approx 6.5\%$ in central Pb-Pb collisions. Particle identification on a track-by-track basis is possible in the region of momentum where particles are well separated by more than 3σ . This allows the identification of pions, kaons and (anti-)protons within the transverse momentum ranges 0.25–0.70 GeV/c, 0.25–0.45 GeV/c, and 0.45–0.90 GeV/c, respectively.

The TPC dE/dx signal in the relativistic rise region ($3 < \beta\gamma \ll 1000$), where the average energy loss increases as $\ln(\beta\gamma)$, allows identification of charged pions, kaons, and (anti-)protons from $p_T \approx 2$ –3 GeV/c up to $p_T = 20$ GeV/c. The first step of the TPC high- p_T analysis is the calibration of the PID signal; a detailed description of the the dE/dx calibration procedure can be found in Refs. [28,35]. Particle identification requires precise knowledge of the $\langle dE/dx \rangle$

response and resolution σ . This is achieved using the PID signals of pure samples of secondary pions and protons originating from K_S^0 and Λ decays as well as a sample of tracks selected with TOF. In addition, measured K_S^0 spectra are used to further constrain the TPC charged kaon response [28]. For different momentum intervals, a sum of four Gaussian functions associated with the pion, kaon, proton and electron signals is fitted to the dE/dx distribution.

d. HMPID analysis. The HMPID performs identification of charged hadrons based on the measurement of the emission angle of Cherenkov radiation. Starting from the association of a track to the MIP cluster centroid one has to reconstruct the photon emission angle. Background, due to other tracks, secondaries and electronic noise, is discriminated exploiting the Hough Transform Method (HTM) [69]. Particle identification with the HMPID is based on statistical unfolding. In pp collisions, a negligible background allows for the extraction of the particle yields from a three-Gaussian fit to the Cherenkov angle distributions in a narrow transverse momentum range. In the case of Pb-Pb collisions, the Cherenkov angle distribution for a narrow transverse momentum bin is described by the sum of three Gaussian distributions for π^\pm , K^\pm , and $(\bar{p})p$ for the signal and a sixth-order polynomial function for the background [28].

This background is due to misidentification in the high occupancy events: the larger the angle, the larger the probability to find background clusters arising from other tracks or photons in the same event. This background is uniformly distributed on the chamber plane. The resolution in Pb-Pb events is the same as in pp collisions (≈ 4 mrad at $\beta \approx 1$). In this analysis, the HMPID provides results in pp and Pb-Pb collisions in the transverse momentum ranges 1.5–4.0 GeV/ c for π^\pm and K^\pm , and in 1.5–6.0 GeV/ c for $(\bar{p})p$.

e. Kink analysis. In addition to the particle identification techniques mentioned above, charged kaons can also be identified in the TPC using the kink topology of their two-body decay mode (e.g., $K \rightarrow \mu + \nu_\mu$) [59]. With the available statistics, this technique extends PID of charged kaons up to 4 GeV/ c in pp collisions and up to 6 GeV/ c in Pb-Pb collisions. The kink analysis reported here is applied for the first time to Pb-Pb data. For the reconstruction of kaon kink decays, the algorithm is implemented within the fiducial volume of the TPC detector ($130 < R < 200$ cm), to ensure that an adequate number of clusters is found to reconstruct the tracks of both the mother and the daughter with the necessary precision to be able to identify the particles. The mother tracks of the kinks are selected using similar criteria as for other primary tracks, except that the minimum number of TPC clusters required are 30 instead of 70, because they are shorter compared to the primary ones. Assuming the neutrino to be massless, the invariant mass of the decayed particle ($M_{\mu\nu}$) is estimated from the charged decay product track and the momentum of the neutrino as reported in Ref. [59]. The main background is from charged pion decays, $\pi \rightarrow \mu + \nu_\mu$ (B.R. = 99.99%), which also gives rise to a kink topology. A proper q_T selection, where q_T is the transverse momentum of the daughter track with respect to the mother's direction at the kink, can separate most of the pion kink background from the kaon kinks. Since the upper limit of q_T values for the decay channels

$\pi \rightarrow \mu + \nu_\mu$ and $K \rightarrow \mu + \nu_\mu$ are 30 MeV/ c and 236 MeV/ c , respectively, a selection of $q_T > 120$ MeV/ c rejects more than 80% (85% in pp collisions) of the pion background. For further removal of the contamination from pion decays, an additional selection on kink opening angle, as reported in Ref. [59], has been implemented. Finally, the TPC dE/dx of the mother tracks is required to have $|N_\sigma^K| < 3$, which improves the purity of the sample. After these selections, the purity ranges from 99% at low p_T to 92% (96% in pp collisions) at high p_T according to Monte Carlo studies. The remaining very low background is coming from random associations of charged tracks reconstructed as fake kinks. After applying all these topological selection criteria, the invariant mass of kaons ($M_{\mu\nu}$) obtained from the reconstruction of their decay products integrated over the above mentioned mother momentum ranges for pp and Pb-Pb collisions are shown in Fig. 2.

B. Correction of raw spectra

To obtain the p_T distributions of primary π^\pm , K^\pm , and $(\bar{p})p$, the raw spectra are corrected for PID efficiency, misidentification probability, acceptance, and tracking efficiencies, following the procedures described in Ref. [14] for the ITS, TPC (low p_T) and TOF, in Ref. [28] for the HMPID and TPC (high p_T) and in Ref. [59] for the kink analysis. The acceptance, reconstruction, and tracking efficiencies are obtained from Monte Carlo simulated events generated with PYTHIA 8.1 (Monash 2013 tune) [70] for pp collisions and with HIJING [71] for Pb-Pb collisions. The particles are propagated through the detector using the GEANT 3 transport code [72], where the detector geometry and response, as well as the data taking conditions, are reproduced in detail. Since GEANT 3 does not describe well the interaction of low-momentum \bar{p} and K^- with the material, a correction to the efficiencies is estimated using GEANT 4 and FLUKA, respectively, which are known to describe such processes better [14,73–75]. The PID efficiency and the misidentification probability are evaluated by performing the analysis on the Monte Carlo simulation, which requires that the simulated data are first tuned to reproduce the real PID response for each PID technique. The contamination due to weak decays of light flavor hadrons (mainly K_S^0 affecting π^\pm spectra, Λ and Σ^+ affecting $(\bar{p})p$ spectra) and interactions with the material has to be computed and subtracted from the raw spectra. Since strangeness production is underestimated in the event generators and the interactions of low p_T particles with the material are not properly modeled in the transport codes, the secondary-particle contribution is evaluated with a data-driven approach. For each PID technique and species, the contribution of feed-down in a given p_T interval is extracted by fitting the measured distributions of DCA_{xy} of the tracks identified as the given hadron species. The DCA_{xy} distributions are modeled with three contributions: primary particles, secondary particles from weak decays of strange hadrons and secondary particles produced in the interactions with the detector material. Their shapes are extracted for each p_T interval and particle species from the Monte Carlo simulation described above. The contribution of secondaries

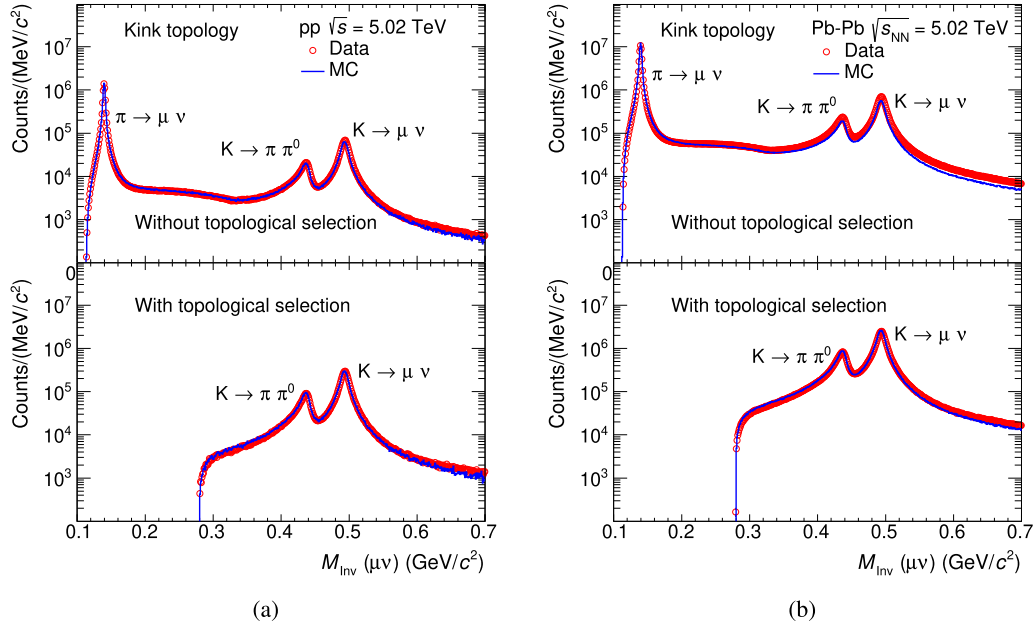


FIG. 2. Invariant mass distribution of identified charged kaons from their decay products in pp (a) and Pb-Pb collisions (b) at $\sqrt{s_{NN}} = 5.02$ TeV. The red circles and blue lines represent the experimental data and Monte Carlo simulation, respectively, before (upper) and after (lower) the topological selection. The peak centered at $M_{\mu\nu} = 0.49$ GeV/c^2 is for the decay channel $K \rightarrow \mu + \nu_{\mu}$ (B.R. = 63.55%), whereas the peak centered at $M_{\mu\nu} = 0.43$ GeV/c^2 is for the decay channel $K \rightarrow \pi + \pi^0$ (B.R. = 20.66%), whose invariant mass is calculated with the wrong mass hypothesis.

is different for each PID analysis due to the different track and PID selections and is more important at low p_T . The measured Pb-Pb spectra are then normalized to the number of events in each centrality class.

The spectra measured in pp collisions are also normalized to the number of inelastic collisions obtained from the number of analyzed minimum bias events corrected with an inelastic normalization factor of $0.757 (\pm 2.51\%)$, defined as the ratio between the V0 visible cross section and the inelastic pp cross section at $\sqrt{s} = 5.02$ TeV [39].

C. Systematic uncertainties

The evaluation of systematic uncertainties follows the procedures described in Ref. [14] for the ITS, TPC (low p_T), and TOF analyses, in Ref. [28] for the HMPID and TPC (high p_T) analyses and in Ref. [59] for the kink analysis. The main sources of systematic uncertainties, for each analysis, are summarized in Tables II and III, for the Pb-Pb and pp analyses, respectively. Sources of systematic effects such as the different PID techniques, the feed-down correction, the imperfect description of the material budget in the Monte Carlo simulation, the knowledge of the hadronic interaction cross section in the detector material, the TPC-TOF and ITS-TPC matching efficiency, and the track selection have been taken into account. The systematic uncertainties related to track selection were evaluated by varying the criteria used to select single tracks (number of reconstructed crossed rows in the TPC, number of available clusters in the ITS, DCA_{xy} and DCA_z , χ^2/NDF of the reconstructed track). The ratio of the corrected spectra with modified selection criteria to the default case is computed to estimate the systematic uncer-

tainty for a given source. A similar approach is used for the evaluation of the systematic uncertainties related to the PID procedure. The uncertainties due to the imperfect description of the material budget in the Monte Carlo simulation is estimated varying the material budget in the simulation by $\pm 7\%$. To account for the effect related to the imperfect knowledge of the hadronic interaction cross section in the detector material, different transport codes (GEANT3, GEANT4, and FLUKA) are compared. Finally, the uncertainties due to the feed-down correction procedure are estimated for all analyses by varying the range of the DCA_{xy} fit, by using different track selections, by applying different cuts on the (longitudinal) DCA_z , and by varying the particle composition of the Monte Carlo templates used in the fit.

For the ITS analysis, the standard N_{σ} method is compared with the yields obtained with a Bayesian PID technique [76]. Moreover, the Lorentz force causes shifts of the cluster position in the ITS, pushing the charge in opposite directions when switching the polarity of the magnetic field of the experiment ($E \times B$ effect) [14]. This effect is not fully reproduced in the Monte Carlo simulation and has been estimated by analyzing data samples collected with different magnetic field polarities. To estimate possible systematic effects deriving from signal extraction in the low p_T TPC analysis, the yield was computed by varying the selection based on the number of TPC crossed rows from 70 to 90 and the yield was computed from the sum of the bin content of the N_{σ} distribution in the range $[-3, 3]$, instead of fitting.

The systematic uncertainty was obtained from the comparison to the nominal yield. Regarding the TPC analysis at high p_T , the imprecise knowledge of both the Bethe-Bloch

TABLE II. Main sources and values of the relative systematic uncertainties (expressed in %) of the p_T -differential yields of π^\pm , K^\pm , and $(\bar{p})p$ obtained in the analysis of Pb-Pb collisions. When two values are reported, these correspond to the lowest and highest p_T bin of the corresponding analysis, respectively. If only one value is reported, then the systematic uncertainty is not p_T -dependent. If not specified, then the uncertainty is not centrality-dependent. The first three systematic uncertainties are common to all PID techniques. The maximum (among centrality classes) total systematic uncertainties and the centrality-independent ones are also shown.

Effect	π^\pm (%)	K^\pm (%)	p and \bar{p} (%)	K/π (%)	p/π (%)
Event selection	0.1	0.1	0.1	—	—
ITS–TPC matching efficiency	0.2–1.2	0.2–1.2	0.2–1.2	—	—
Material budget	1.6–0.2	1.3–0.4	2.9–0.1	2.0–0.4	3.2–0.3
Hadronic interaction cross section	2.5–2.4	2.7–1.8	4.6	3.3–3.0	5.0–5.2
ITS PID	1.9–5.7	0.8–3.1	3.4–2.7	1.8–3.8	4.1–4.4
Track selection	2.0–2.1	2.6–2.3	4.9–4.4	1.6–1.1	4.1–3.5
$E \times B$	3.0	3.0	3.0	4.2	4.2
Feed-down correction	1.1	—	0.4	1.1	1.2
Matching efficiency (0–5%)	2.8	2.8	2.8	—	—
Matching efficiency (40–50%)	1.9	1.9	1.9	—	—
Matching efficiency (80–90%)	0.5	0.5	0.5	—	—
Hadronic interaction cross section (ITS tracks)	2.0	2.7–1.5	4.6–2.0	3.3–2.5	5.0–2.8
Low- p_T TPC PID (0–5%)	2.7–8.3	3.0–10.0	3.2–13.6	6.0–16.0	8.0–18.0
Low- p_T TPC PID (40–50%)	2.2–6.0	2.5–6.0	2.1–9.3	2.0–11.0	3.0–13.0
Low- p_T TPC PID (80–90%)	4.5–6.8	3.0–6.8	3.3–8.3	4.0–11.0	8.0–11.0
Track selection	1.0–5.0	1.0–5.0	1.0–5.0	—	—
Feed-down correction	1.0	—	2.5	1.2–0.4	10.0–5.0
TOF PID	3.0–12.0	3.0–18.0	2.0–20.0	2.0–15.0	2.0–20.0
Track selection	1.5	1.5	1.8	2.0	1.5
Matching efficiency	4.0	4.0	4.0	—	—
Feed-down correction	0.5–0.2	—	1.0–0.5	0.5–0.2	0.5–1.5
HMPID PID	3.0–11.0	2.0–11.0	2.0–11.0	3.0–11.5	2.0–11.5
Track selection	4.5	4.5	4.5	3.6	3.6
PID efficiency correction	5.0	5.0	5.0	5.0	5.0
Distance selection correction (matching efficiency)	2.0	2.0	4.0–2.0	1.0	1.0
Feed-down correction	0.1	—	0.3	0.2	0.3
Background (0–5%)	18.0–6.0	10.0–2.0	10.0–1.5	10.0–2.0	10.0–2.0
Background (30–40%)	10.0–1.0	5.0–1.0	5.0–1.0	6.0–1.5	6.0–1.5
Background (60–70%)	4.0–1.0	2.0–1.0	2.0–1.0	3.0–1.0	3.0–1.0
High- p_T TPC Bethe-Bloch param. (0–5%)	4.2–2.0	22.3–8.5	13.1–8.0	21.9–8.0	11.4–10.0
High- p_T TPC Bethe-Bloch param. (40–50%)	4.3–2.0	17.0–8.5	16.3–8.0	17.1–8.0	15.6–10.0
High- p_T TPC Bethe-Bloch param. (80–90%)	2.9–2.0	11.4–8.5	21.1–7.9	11.9–8.0	20.3–10.0
Track selection (0–5%)	1.5–1.1	1.5–1.1	1.5–1.1	—	—
Track selection (40–50%)	1.0–0.7	1.0–0.7	1.0–0.7	—	—
Track selection (80–90%)	0.7–1.7	0.7–1.7	0.7–1.7	—	—
p_T resolution	0.0–0.3	0.0–0.3	0.0–0.3	—	—
Feed-down correction	0.4–0.4	—	3.0–2.6	—	3.0–2.6
Kink PID + reconstruction efficiency (0–5%)	—	1.0–10.4	—	—	—
Kink PID + reconstruction efficiency (30–40%)	—	0.5–4.5	—	—	—
Kink PID + reconstruction efficiency (80–90%)	—	0.7–5.5	—	—	—
Track selection	—	3.0	—	—	—
Contamination (0–5%)	—	0.6–5.0	—	—	—
Contamination (30–40%)	—	0.6–5.0	—	—	—
Contamination (80–90%)	—	0.6–4.0	—	—	—
Total	7.3–3.9	5.9–9.8	9.7–9.2	7.7–8.0	9.9–11.0
Total (N_{ch} -independent)	7.0–2.7	5.5–9.4	9.2–8.7	7.2–8.0	9.4–9.2

and resolution parametrizations constitutes the most significant source of systematic uncertainties associated with the signal extraction. To quantify the size of the uncertainty, the relative variations of dE/dx and resolution with respect to

the original parametrizations were used. The TOF analysis estimates the PID systematic uncertainties by comparing the standard spectra with the ones extracted from a statistical deconvolution, which is based on templates generated from

TABLE III. Main sources and values of the relative systematic uncertainties (expressed in %) of the p_T -differential yields of π^\pm , K^\pm , and $(\bar{p})p$ obtained in the analysis of pp collisions. When two values are reported, these correspond to the lowest and highest p_T bin of the corresponding analysis, respectively. If only one value is reported, then the systematic uncertainty is not p_T -dependent. The first three systematic uncertainties are common to all PID techniques. In the last row, the total systematic uncertainty is reported.

Effect	π^\pm (%)	K^\pm (%)	p and \bar{p} (%)	K/π (%)	p/π (%)
Event selection	0.5	0.5	0.5	—	—
ITS-TPC matching efficiency	0.0–1.1	0.0–1.1	0.0–1.1	—	—
Material budget	1.6–0.2	2.0–0.4	2.9–0.1	2.4–0.4	3.2–0.3
Hadronic interaction cross section	2.5–2.4	2.7–1.8	4.6	3.3–3.0	5.0–5.2
ITS PID	1.5–6.4	0.4–5.7	1.2–1.5	0.9–7.4	1.5–1.9
Track selection	2.6–2.1	2.5–3.8	3.0–2.0	1.8–0.5	2.5–1.7
Feed-down correction	—	—	1.6	—	1.6
$E \times B$	3.0	3.0	3.0	4.2	4.2
Hadronic interaction cross section (ITS tracks)	2.0	2.7–1.8	4.6–2.0	3.3–2.7	5.0–2.8
Low- p_T TPC PID	5.7–8.3	4.6–7.9	9.2–13.2	5.0–9.0	10.0–15.0
Track selection	1.0–4.0	1.0–4.0	1.0–4.0	—	—
Feed-down correction	1.0	—	2.0	1.1–0.6	5.0–2.0
TOF PID	1.0–8.0	1.2–15.0	1.0–15.0	2.0–20.0	2.0–20.0
Track selection	1.5	1.5	2.0	2.0	3.0
Matching efficiency	1.0	1.0	1.0	—	—
Feed-down correction	0.5–0.1	—	1–0.5	0.5–0.1	0.2–0.5
HMPID PID	3.0–11.0	2.0–11.0	2.0–11.0	3.0–11.5	2.0–11.5
Track selection	4.5	4.5	4.5	3.6	3.6
Distance selection correction (matching efficiency)	2.0	2.0	4.0–2.0	1.0	1.0
Feed-down correction	0.1	—	0.3	0.2	0.3
High- p_T TPC Bethe-Bloch parametrization	2.4–2.0	14.5–8.0	22.0–12.0	15.1–8.0	22.5–15.0
Track selection	0.9–1.7	0.9–1.7	0.9–1.7	—	—
p_T resolution	0.0–0.3	0.0–0.3	0.0–0.3	—	—
Feed-down correction	0.0–0.3	—	1.9–1.7	—	1.9–1.7
Kink PID + reconstruction efficiency	—	4.3	—	—	—
Track selection	—	3.0	—	—	—
Contamination	—	0.2–3.2	—	—	—
Total	6.4–3.4	4.6–9.2	6.9–12.5	4.9–8.0	6.7–15.1

a TOF time response function with varied parameters. For the HMPID analysis, the selection on the distance between the extrapolated track point at the HMPID chamber planes and the corresponding MIP cluster centroid, $d_{\text{MIP-trk}}$, is varied by ± 1 cm to check its systematic effect on the matching of tracks with HMPID signals. Moreover, the systematic bias due to the background fitting, which represents the largest source, is estimated by changing the fitting function: from a sixth-order polynomial to a power law of the tangent of the Cherenkov angle. This function is derived from geometrical considerations [77]. For the kink analysis, the systematic uncertainties are estimated by comparing the standard spectra with the ones obtained by varying the selection on decay product transverse momentum, the minimum number of TPC clusters, kink radius and TPC N_σ values of the mother tracks.

By using the same methods as for the spectra, the systematic uncertainties for the p_T -dependent particle ratios were computed to take into account the correlated sources of uncertainty (mainly due to PID and tracking efficiency). Finally, for both p_T -dependent spectra and ratios the particle-multiplicity-dependent systematic uncertainties, those that are uncorrelated across different centrality bins, were determined.

The improved reconstruction and track selection in the analysis of pp and Pb-Pb data at $\sqrt{s_{NN}} = 5.02$ TeV lead to reduced systematic uncertainties as compared to previously published results at $\sqrt{s_{NN}} = 2.76$ TeV.

III. RESULTS AND DISCUSSION

The measured p_T spectra of π^\pm , K^\pm , and $(\bar{p})p$ from the independent analyses have to be combined in the overlapping ranges using a weighted average with the systematic and statistical uncertainties as weights. All the systematic uncertainties are considered to be uncorrelated across the different PID techniques apart from those related to the ITS-TPC matching efficiency and the event selection. The correlated systematic uncertainties have been added in quadrature after the spectra have been combined. For a given hadron species, the spectra of particles and antiparticles are found to be compatible, and therefore all spectra reported in this section are shown for summed charges.

Figure 3 shows the combined p_T spectra of π^\pm , K^\pm , and $(\bar{p})p$ measured in 0–90% Pb-Pb and inelastic pp collisions at $\sqrt{s_{NN}} = 5.02$ TeV. Results for Pb-Pb collisions are presented

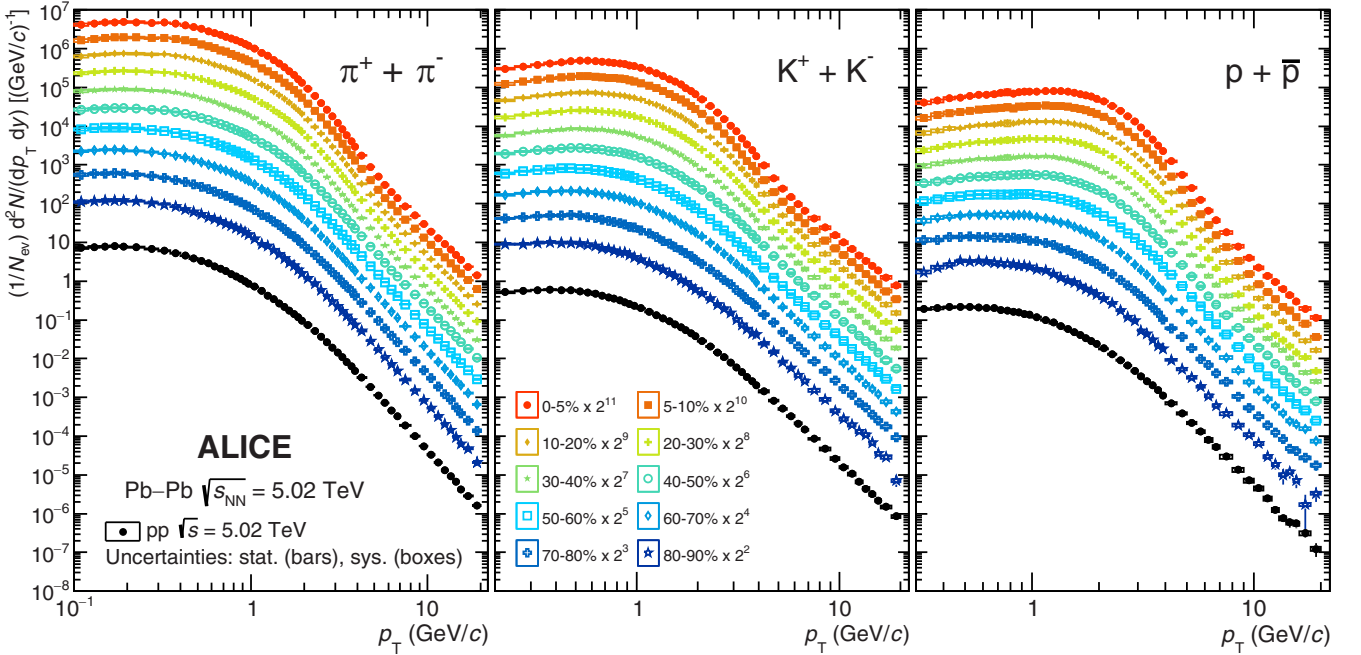


FIG. 3. Transverse momentum spectra of pions (left), kaons (middle), and (anti-)protons (right) measured in Pb-Pb collisions at $\sqrt{s_{NN}} = 5.02$ TeV for different centrality classes. Scale factors are applied for better visibility. The results are compared with the spectra measured in inelastic pp collisions at $\sqrt{s} = 5.02$ TeV. Statistical and systematic uncertainties are displayed as error bars and boxes around the data points, respectively.

for different centrality classes. Scaling is applied in the plots to improve spectra visibility. In the low p_T region, the maximum of the spectra is pushed toward higher momenta while going from peripheral to central Pb-Pb events. This effect is mass dependent and can be interpreted as a signature of radial flow [14]. For high p_T , the spectra follow a power-law shape, as expected from perturbative QCD (pQCD) calculations [78].

The p_T -integrated yields, dN/dy , and the average transverse momentum, $\langle p_T \rangle$, are determined for the different centrality classes using an extrapolation to $p_T = 0$. The extrapolation procedure is performed after fitting the measured spectra with Boltzmann-Gibbs Blast-Wave [79] (for Pb-Pb) or the Lévy-Tsallis [80,81] (for pp) functions. In the most central Pb-Pb collisions (0–5%), the extrapolated fractions of the total yields are 5.84%, 5.20%, and 3.72%, for pions, kaons, and (anti-)protons, respectively. The fractions increase as centrality decreases, reaching 8.63%, 9.36%, and 10.73% in the most peripheral collisions (80–90%). In pp collisions the fractions are 8.59%, 9.98%, and 12.61% for pions, kaons, and (anti-)protons, respectively. The systematic uncertainties are then propagated to the p_T -integrated yields and mean transverse momentum. For the uncertainty on dN/dy , the fit is performed with all data points shifted up by their full systematic uncertainties. To estimate the uncertainty on $\langle p_T \rangle$, points in the 0–3 GeV/c range are shifted up and down within their systematic uncertainty to obtain the softest and hardest spectra. The maximum difference (in absolute value) between the integrated quantities obtained with the standard and modified spectra are included as part of the systematic uncertainty.

Additionally, different functions¹ were used to perform the extrapolation and the largest differences were added to the previous contributions.

The statistical uncertainties on the dN/dy and $\langle p_T \rangle$ values are evaluated propagating the uncertainties on the fit parameters obtained directly from the fit procedure. The procedure described above is repeated using the systematic uncertainties uncorrelated across different centrality bins to extract the centrality uncorrelated part of the systematic uncertainties on the p_T -integrated particle yields and the average transverse momenta.

In Table IV, the dN/dy and $\langle p_T \rangle$ are shown for Pb-Pb and pp collisions, respectively. For Pb-Pb collisions the values are given for different centrality ranges.

A. Particle production at low transverse momentum

The Boltzmann-Gibbs blast-wave function is a three-parameter simplified hydrodynamic model in which particle production is given by [79]

$$E \frac{d^3N}{dp^3} \propto \int_0^R m_T I_0 \left(\frac{p_T \sinh(\rho)}{T_{\text{kin}}} \right) K_1 \left(\frac{m_T \cosh(\rho)}{T_{\text{kin}}} \right) r dr. \quad (4)$$

¹Lévy-Tsallis (Pb-Pb only); Boltzmann-Gibbs blast-wave (pp only); m_T -exponential: $Ax \times \exp(-\sqrt{x^2 + m^2}/T)$, where A is a normalization constant, T the temperature, and m the mass; Fermi-Dirac $Ax \times 1/(\exp(\sqrt{x^2 + m^2}/T) + 1)$; Bose-Einstein $Ax \times 1/(\exp(\sqrt{x^2 + m^2}/T) - 1)$; Boltzmann $Ax \times \sqrt{x^2 + m^2} \times \exp(-\sqrt{x^2 + m^2}/T)$.

TABLE IV. dN/dy and $\langle p_T \rangle$ measured in Pb-Pb and pp collisions at $\sqrt{s_{NN}} = 5.02$ TeV. Pb-Pb results are shown for the different centrality classes. Statistical and systematic uncertainties are also reported.

$\pi^+ + \pi^-$						
Centrality class	dN/dy	Stat. Uncert.	Syst. Uncert.	$\langle p_T \rangle$	Stat. Uncert.	Syst. Uncert.
0–5%	1699.80	0.88	116.91	0.5682	0.0002	0.0320
5–10%	1377.49	0.71	66.90	0.5711	0.0002	0.0181
10–20%	1039.47	0.46	47.36	0.5704	0.0002	0.0174
20–30%	712.92	0.34	36.06	0.5615	0.0002	0.0192
30–40%	467.76	0.26	23.97	0.5525	0.0002	0.0198
40–50%	292.91	0.19	15.80	0.5389	0.0003	0.0206
50–60%	171.14	0.18	9.77	0.5214	0.0004	0.0215
60–70%	88.82	0.10	5.21	0.5082	0.0004	0.0205
70–80%	41.69	0.07	2.49	0.4924	0.0006	0.0203
80–90%	16.31	0.04	0.91	0.4775	0.0008	0.0178
$K^+ + K^-$						
Centrality class	dN/dy	Stat. Uncert.	Syst. Uncert.	$\langle p_T \rangle$	Stat. Uncert.	Syst. Uncert.
0–5%	273.41	0.35	11.62	0.9177	0.0009	0.0140
5–10%	222.48	0.54	9.37	0.9214	0.0018	0.0130
10–20%	168.16	0.24	6.89	0.9193	0.0010	0.0126
20–30%	114.70	0.15	4.67	0.9052	0.0008	0.0114
30–40%	75.00	0.09	2.96	0.8919	0.0008	0.0106
40–50%	46.36	0.06	1.88	0.8685	0.0009	0.0113
50–60%	26.38	0.05	1.09	0.8369	0.0011	0.0132
60–70%	13.38	0.03	0.64	0.8165	0.0015	0.0138
70–80%	6.01	0.02	0.30	0.7881	0.0019	0.0160
80–90%	2.27	0.01	0.12	0.7541	0.0032	0.0179
$p + \bar{p}$						
Centrality class	dN/dy	Stat. Uncert.	Syst. Uncert.	$\langle p_T \rangle$	Stat. Uncert.	Syst. Uncert.
0–5%	74.56	0.06	3.75	1.4482	0.0007	0.0244
5–10%	61.51	0.07	2.93	1.4334	0.0009	0.0224
10–20%	47.40	0.04	2.20	1.4143	0.0007	0.0216
20–30%	33.17	0.04	1.50	1.3768	0.0008	0.0199
30–40%	22.51	0.03	1.01	1.3209	0.0010	0.0177
40–50%	14.46	0.02	0.66	1.2570	0.0012	0.0179
50–60%	8.71	0.02	0.40	1.1822	0.0016	0.0151
60–70%	4.74	0.01	0.27	1.1004	0.0022	0.0184
70–80%	2.30	0.01	0.14	1.0181	0.0030	0.0221
80–90%	0.92	0.01	0.06	0.9464	0.0053	0.0277
pp collisions						
Particle specie	dN/dy	Stat. Uncert.	Syst. Uncert.	$\langle p_T \rangle$	Stat. Uncert.	Syst. Uncert.
$\pi^+ + \pi^-$	4.1342	0.0005	0.3032	0.4582	0.0001	0.0284
$K^+ + K^-$	0.5343	0.0014	0.0273	0.7412	0.0008	0.0296
$p + \bar{p}$	0.2331	0.0002	0.0205	0.8820	0.0006	0.0498

The velocity profile ρ is given by

$$\rho = \tanh^{-1} \beta_T = \tanh^{-1} \left[\left(\frac{r}{R} \right)^n \beta_s \right], \quad (5)$$

where β_T is the radial expansion velocity, m_T the transverse mass ($m_T = \sqrt{m^2 + p_T^2}$), and T_{kin} the temperature at the kinetic freeze-out, I_0 and K_1 are the modified Bessel functions, r is the radial distance in the transverse plane, R is the radius of the fireball, β_s is the transverse expansion velocity at the surface, and n is the exponent of the velocity profile.

To quantify the centrality dependence of spectral shapes at low p_T , the Boltzmann-Gibbs blast-wave function has been simultaneously fitted to the charged pion, kaon and (anti-)proton p_T spectra, using a common set of parameters but different normalization factors and masses. Although the absolute values of the parameters have a strong dependence on the p_T range used for the fit [14], the evolution of the parameters with $\sqrt{s_{NN}}$ can still be compared across different collision energies by using the same fitting ranges. The present analysis uses the same p_T intervals employed for fitting as in a previous

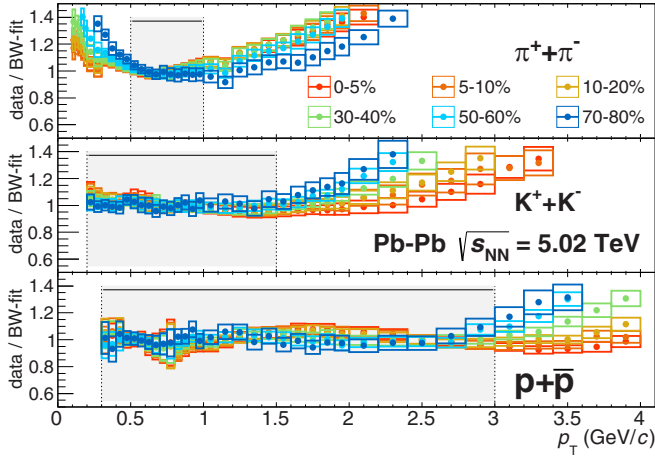


FIG. 4. Ratios of centrality-dependent p_T spectra to model (blast-wave parametrization) predictions in Pb-Pb collisions at $\sqrt{s_{NN}} = 5.02$ TeV for pions (top), kaons (middle) and protons (bottom). The fit ranges are indicated as gray shaded areas.

publication [14], namely, 0.5–1 GeV/c, 0.2–1.5 GeV/c, and 0.3–3 GeV/c for charged pions, kaons, and (anti-)protons, respectively. Figure 4 shows the ratios of the spectra to results of the fits for different centrality classes and particle species. If the shape of the p_T distributions over the full measured p_T range was purely driven by the collective radial expansion of the system, then the functions determined by fitting the data in a limited p_T range would be expected to describe the spectral shapes in the full p_T range. Within uncertainties, this is only observed for the proton p_T spectra (up to 4 GeV/c) in 0–20% Pb-Pb collisions. A different situation is observed for pions where, due to their small mass and the large centrality-dependent feed-down contribution from resonance decays, the agreement with the model is worse than that observed for kaons and (anti-)protons.

The p_T interval where the model describes the data within uncertainties gets wider going from peripheral to central Pb-Pb collisions.

TABLE V. Results of the combined Boltzmann-Gibbs blast-wave fits to the particle spectra measured in Pb-Pb collisions at $\sqrt{s_{NN}} = 5.02$ TeV, in the p_T ranges 0.5–1 GeV/c, 0.2–1.5 GeV/c, and 0.3–3.0 GeV/c for π^\pm , K^\pm , and $(\bar{p})p$, respectively. Values in parenthesis refer to the ratios to the values in Pb-Pb collisions at $\sqrt{s_{NN}} = 2.76$ TeV [14]. The charged particle multiplicity values are taken from Refs. [84,85].

Centrality	$\langle dN_{ch}/d\eta \rangle$	$\langle \beta_T \rangle$	T_{kin} (GeV)	n
0–5%	1943 ± 56	(1.018)0.663 \pm 0.003	(0.947)0.090 \pm 0.003	(1.032)0.735 \pm 0.013
5–10%	1587 ± 47	(1.022)0.660 \pm 0.003	(0.938)0.091 \pm 0.003	(1.005)0.736 \pm 0.013
10–20%	1180 ± 31	(1.025)0.655 \pm 0.003	(0.949)0.094 \pm 0.003	(1.001)0.739 \pm 0.013
20–30%	786 ± 20	(1.029)0.643 \pm 0.003	(0.960)0.097 \pm 0.003	(0.990)0.771 \pm 0.014
30–40%	512 ± 15	(1.030)0.622 \pm 0.003	(0.953)0.101 \pm 0.003	(0.985)0.828 \pm 0.015
40–50%	318 ± 12	(1.037)0.595 \pm 0.004	(0.964)0.108 \pm 0.003	(0.962)0.908 \pm 0.019
50–60%	183 ± 8	(1.041)0.557 \pm 0.005	(0.975)0.115 \pm 0.003	(0.957)1.052 \pm 0.024
60–70%	96.3 ± 5.8	(1.035)0.506 \pm 0.008	(1.000)0.129 \pm 0.005	(0.977)1.262 \pm 0.043
70–80%	44.9 ± 3.4	(0.993)0.435 \pm 0.011	(1.058)0.147 \pm 0.006	(1.063)1.678 \pm 0.088
80–90%	17.5 ± 1.8	(0.994)0.355 \pm 0.016	(1.066)0.161 \pm 0.006	(1.071)2.423 \pm 0.208

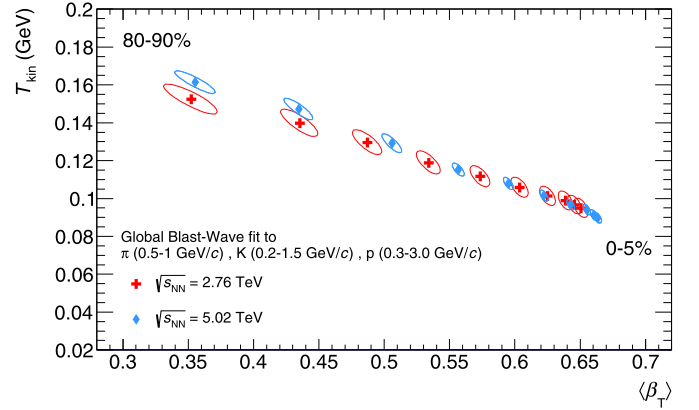


FIG. 5. Average expansion velocity ($\langle \beta_T \rangle$) and kinetic freeze-out temperature (T_{kin}) progression from the simultaneous Boltzmann-Gibbs blast-wave fit to π^\pm , K^\pm , and $p(\bar{p})$ spectra measured in Pb-Pb collisions at $\sqrt{s_{NN}} = 5.02$ and 2.76 TeV [14]. The correlated uncertainties from the global fit are shown as ellipses. The elliptical contours correspond to 1σ uncertainties, with statistical and systematic uncertainties being added in quadrature.

In Table V the blast-wave fit parameters $\langle \beta_T \rangle$, T_{kin} and n in Pb-Pb collisions at $\sqrt{s_{NN}} = 5.02$ TeV, for different centrality classes, are listed. Figure 5 shows the correlation between $\langle \beta_T \rangle$ and T_{kin} , both obtained from the simultaneous fit for Pb-Pb collisions at $\sqrt{s_{NN}} = 2.76$ TeV and 5.02 TeV. For Pb-Pb collisions at $\sqrt{s_{NN}} = 5.02$ TeV, $\langle \beta_T \rangle$ increases with centrality, reaching $\langle \beta_T \rangle = 0.663 \pm 0.003$ in 0–5% central collisions, while T_{kin} decreases from $T_{kin} = (0.161 \pm 0.006)$ GeV to $T_{kin} = (0.090 \pm 0.003)$ GeV, similarly to what was observed at lower energies. This can be interpreted as a possible indication of a more rapid expansion with increasing centrality [4,14]. In peripheral collisions this is consistent with the expectation of a shorter lived fireball with stronger radial pressure gradients [82]. The value of the exponent of the velocity profile of the expansion, n , is about 0.74 in central collisions and it increases up to 2.52 in peripheral collisions (see Table V). The values of n in peripheral collisions increase with respect to those in central collisions to reproduce the

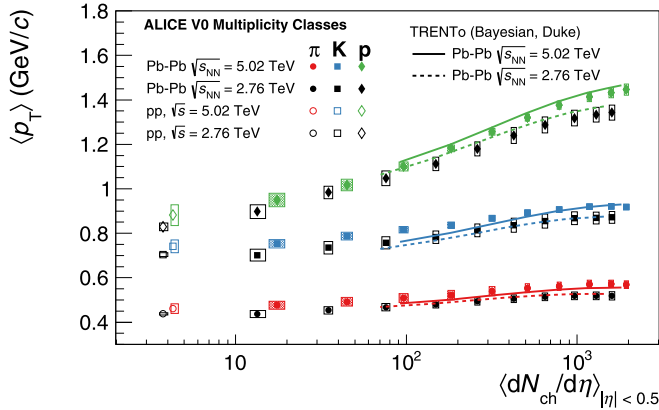


FIG. 6. Mean transverse momentum as a function of $\langle dN_{ch}/d\eta \rangle$ for π^\pm , K^\pm , and $(\bar{p})p$ in Pb-Pb collisions at $\sqrt{s_{NN}} = 5.02$ (full color markers) and 2.76 TeV [14] (full black markers) and in inelastic pp collisions at $\sqrt{s} = 5.02$ and 2.76 TeV (empty color markers) [59]. The empty boxes show the total systematic uncertainty; the shaded boxes indicate the contribution uncorrelated across centrality bins (not estimated in Pb-Pb collisions at $\sqrt{s_{NN}} = 2.76$ TeV). Continuous lines represent the Bayesian analysis predictions.

power-law tail of the p_T spectra. Finally, in the most central Pb-Pb (0–5%) collisions the difference of the average transverse velocity between the two collision energies is ≈ 2.4 standard deviations.

The value at 5.02 TeV is $\approx 2\%$ larger than that measured at 2.76 TeV, whereas the kinetic freeze-out temperature results are slightly smaller at larger collision energy but the difference is not significant. Just for the most peripheral collisions the kinetic freeze-out temperature is slightly higher at 5.02 TeV than that at 2.76 TeV. This is in contrast with our interpretation for central collisions where a larger volume has the kinetic freeze-out later allowing the kinetic temperature to decrease further. It is worth questioning whether the blast wave formalism is applicable also for these smaller system and it will be interesting to see if models, which can also describe small systems, can explain this changing pattern. Moreover, we note that event and geometry biases may also play a role in the peripheral Pb-Pb collisions [83].

Figure 6 shows the $\langle p_T \rangle$ for charged pions, kaons, and (anti-)protons as a function of the charged particle multiplicity density $\langle dN_{ch}/d\eta \rangle$ at midrapidity in Pb-Pb collisions at $\sqrt{s_{NN}} = 5.02$ and 2.76 TeV. Going from inelastic pp collisions to peripheral and central Pb-Pb collisions, the $\langle p_T \rangle$ increases with $\langle dN_{ch}/d\eta \rangle$. The rise of the average p_T gets steeper with increasing hadron mass, this effect is consistent with the presence of radial flow. Within uncertainties and for comparable charged particle multiplicity densities, the results for both energies are consistent for 20–90% Pb-Pb collisions. For 0–20% Pb-Pb collisions, $\langle p_T \rangle$ is slightly higher at 5.02 TeV than at 2.76 TeV. The increase originates from the low p_T part of the spectra. Again, this is an effect consistent with a stronger radial flow in Pb-Pb collisions at the highest collision energy.

Figure 7 shows the p_T -integrated particle ratios, K/π and p/π , as a function of $\langle dN_{ch}/d\eta \rangle$ in Pb-Pb at

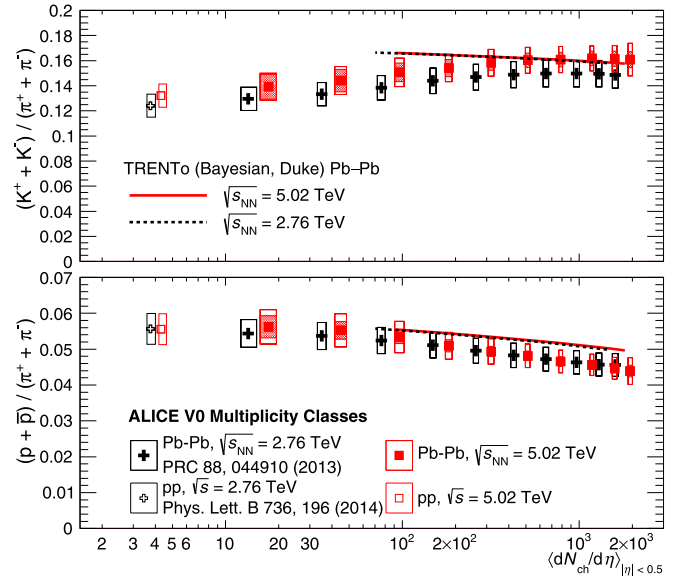


FIG. 7. Transverse momentum integrated K/π (top) and p/π (bottom) ratios as a function of $\langle dN_{ch}/d\eta \rangle$ in Pb-Pb collisions at $\sqrt{s_{NN}} = 5.02$ TeV, compared to Pb-Pb at 2.76 TeV [14]. The values in pp collisions at $\sqrt{s} = 5.02$ and 2.76 TeV are also shown. The empty boxes show the total systematic uncertainty; the shaded boxes indicate the contribution uncorrelated across centrality bins (not estimated in Pb-Pb collisions at $\sqrt{s_{NN}} = 2.76$ TeV). Continuous lines represent the Bayesian analysis predictions.

$\sqrt{s_{NN}} = 2.76$ and 5.02 TeV, and in inelastic pp collisions at $\sqrt{s_{NN}} = 2.76$ and 5.02 TeV. The systematic uncertainties on the integrated ratios have been evaluated using the uncertainties on the p_T -dependent ratios, taking into account the part of the uncertainties correlated among the different particle species. No significant energy dependence is observed, indicating that there is small or no dependence of the hadrochemistry on the collision energy. The K/π ratio hints at a small increase with centrality. The effect is consistent with the observed increase of strange to nonstrange hadron production in heavy-ion collisions compared to inelastic pp collisions [86]. The p/π ratio suggests a small decrease with centrality. Using the centrality uncorrelated uncertainties, the difference between the ratio in the most central (0–5%) and peripheral (80–90%) collisions is ≈ 4.7 standard deviations, thus the difference is significant. The decreasing ratio is therefore consistent with the hypothesis of antibaryon-baryon annihilation in the hadronic phase [16–19,87,88]. The effect is expected to be less important for the more dilute system created in peripheral collisions.

Recently, a new procedure has been implemented to quantitatively estimate properties of the quark-gluon plasma created in ultrarelativistic heavy-ion collisions utilizing Bayesian statistics and a multiparameter model-to-data comparison [89].

The study is performed using a recently developed parametric initial condition model, reduced thickness event-by-event nuclear topology (T_RENTo) [90], which interpolates among a general class of energy-momentum distributions in the initial condition, and a modern hybrid model which

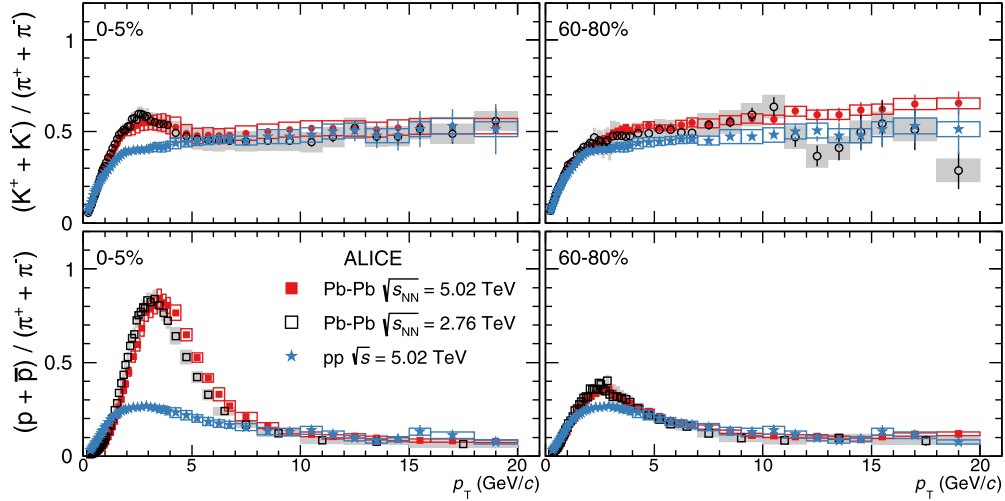


FIG. 8. Centrality dependence of the K/π (top) and p/π (bottom) ratios as a function of transverse momentum, measured in Pb-Pb collisions at $\sqrt{s_{NN}} = 5.02$ and 2.76 TeV [28]. The ratios in pp collisions at $\sqrt{s} = 5.02$ TeV is also shown. The statistical and systematic uncertainties are shown as error bars and boxes around the data points, respectively.

couples viscous hydrodynamics to a hadronic cascade model. The model uses multiplicity, transverse momentum, and flow data from Pb-Pb collisions at $\sqrt{s_{NN}} = 2.76$ TeV to constrain the parametrized initial conditions and the temperature-dependent transport coefficients of the QGP. Based on this set of parameters, predictions for Pb-Pb collisions at $\sqrt{s_{NN}} = 5.02$ TeV are provided. The average transverse momentum and integrated yields in Pb-Pb collisions at $\sqrt{s_{NN}} = 2.76$ TeV are used as input to extract predictions at $\sqrt{s_{NN}} = 5.02$ TeV. The predictions from the multiparameter Bayesian analysis are compared with data in Figs. 6 and 7. The average transverse momentum as a function of $\langle dN_{ch}/d\eta \rangle$ is quite well reproduced by the model. The model predicts that the kaon-to-pion ratio should decrease with increasing charged particle multiplicity density while data show an increase with $\langle dN_{ch}/d\eta \rangle$. Within uncertainties, the model agrees with the data for the most central Pb-Pb collisions. The trend of the proton-to-pion ratio is qualitatively well captured by the model but the values of the centrality-dependent ratios are overestimated.

B. Intermediate transverse momentum

Figure 8 shows the K/π and p/π ratios as a function of p_T for Pb-Pb collisions at $\sqrt{s_{NN}} = 2.76$ and 5.02 TeV. The results are also compared with inelastic pp collisions at $\sqrt{s} = 5.02$ TeV. Within uncertainties, in the K/π ratio, no significant energy dependence is observed in heavy-ion data over the full p_T interval. The ratios measured in 60–80% Pb-Pb collisions at both $\sqrt{s_{NN}}$ agree within systematic uncertainties with that for inelastic pp collisions over the full p_T range. Given that in pp collisions at LHC energies the ratio as a function of p_T does not change with \sqrt{s} [66], and given the similarity between pp and peripheral Pb-Pb collisions, the large difference observed is likely a systematic effect of the measurement and not a physics effect.

In general, the particle ratios exhibit a steep increase with p_T going from 0 to 3 GeV/c while for p_T larger than

10 GeV/c little or no p_T dependence is observed. Going from peripheral to the most central Pb-Pb collisions, the ratios in the region around $p_T \approx 3$ GeV/c are continuously growing. A hint of an enhancement with respect to inelastic pp collisions is observed at $p_T \approx 3$ GeV/c. As pointed out in previous publications [14,28], the effect could be a consequence of radial flow which affects kaons more than pions.

The p/π ratios measured in heavy-ion collisions exhibit a pronounced enhancement with respect to inelastic pp collisions, reaching a value of about 0.8 at $p_T = 3$ GeV/c. This is reminiscent of the increase in the baryon-to-meson ratio observed at RHIC in the intermediate p_T region [45,91]. Such an increase with p_T is due to the mass ordering induced by the radial flow (heavier particles are boosted to higher p_T by the collective motion) and it is an intrinsic feature of hydrodynamical models. It should be noted that this is also suggestive of the interplay of the hydrodynamic expansion of the system with the recombination picture as discussed in the introduction. However, since recombination mainly affects baryon-to-meson ratios, it would not explain the bump which is also observed in the kaon-to-pion ratio. The shift of the peak towards higher p_T in the proton-to-pion ratio is consistent with the larger radial flow measured in Pb-Pb at $\sqrt{s_{NN}} = 5.02$ TeV compared to the one measured at $\sqrt{s_{NN}} = 2.76$ TeV. The mass dependence of the radial flow explains also the observation that the maximum of the p/π ratio is located at a larger p_T as compared to the K/π ratio. The radial flow is expected to be stronger in the most central collisions, this explains the slight shift in the location of the maximum when central and peripheral data are compared. Finally, particle ratios at high p_T in Pb-Pb collisions at both energies become similar to those in pp collisions, suggesting that vacuumlike fragmentation processes dominate there [35].

C. Particle production at high transverse momentum

Figure 9 shows the centrality dependence of R_{AA} as a function of p_T for charged pions, kaons and (anti-)protons.

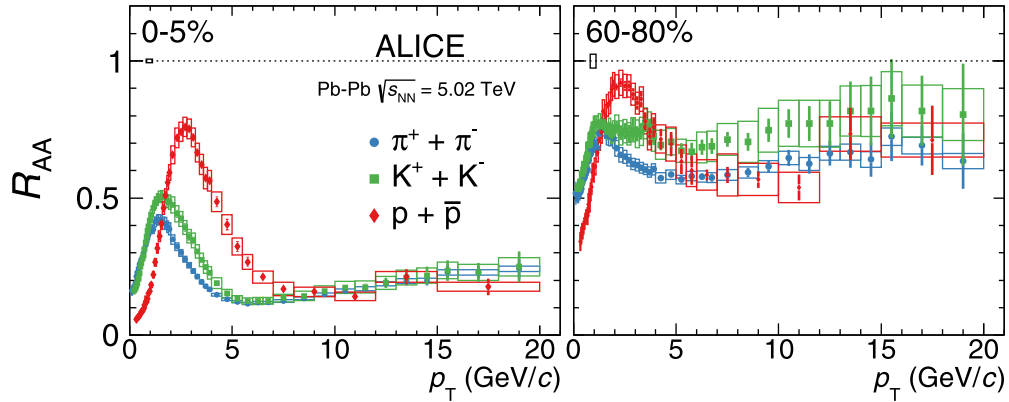


FIG. 9. Centrality dependence of the nuclear modification factor of charged π^\pm , K^\pm , and $(\bar{p})p$ as a function of transverse momentum, measured in Pb-Pb collisions at $\sqrt{s_{NN}} = 5.02$ TeV. The statistical and systematic uncertainties are shown as error bars and boxes around the data points. The total normalization uncertainty (pp and Pb-Pb) is indicated in each panel by the vertical scale of the box centered at $p_T = 1$ GeV/c and $R_{AA} = 1$.

For $p_T < 10$ GeV/c, protons appear to be less suppressed than kaons and pions, consistent with the particle ratios shown in Fig. 8. The large difference between the suppression of different species is consistent with a mass ordering related to the radial flow. It is worth noting that 2.76 TeV measurements [92] showed that the mesons, including $\phi(1020)$, have smaller R_{AA} than protons, indicating a baryon-meson ordering, so while there is a strong radial flow component, there are other effects affecting R_{AA} in this p_T region. At larger p_T , all particle species are equally suppressed. Despite the strong energy loss observed in the most central heavy-ion collisions, particle composition and ratios at high p_T are similar to those in vacuum. This suggests that jet quenching does not affect particle composition significantly.

In the identified particle R_{AA} for peripheral Pb-Pb collisions an apparent presence of jet quenching is observed ($R_{AA} < 1$), although for similar particle densities in smaller systems

(like p -Pb collisions) no jet quenching signatures have been reported [93]. It has been argued that peripheral A - A collisions can be significantly affected by event selection and geometry biases [83], leading to an apparent suppression for R_{AA} even if jet quenching and shadowing are absent. The presence of biases on the R_{AA} measurement in peripheral Pb-Pb collisions has been confirmed in Ref. [94]: the geometry bias sets in at mid-central collisions, reaching about 15% for the 70–80% Pb-Pb collisions. The additional effect of the selection bias becomes noticeable above the 60% percentile and is significant above the 80% percentile, where it is larger than 20%. All hard probes should be similarly affected [83], in particular, the leading pions, kaons and (anti-)protons reported in the present paper.

Figure 10 shows the R_{AA} for charged pions, kaons and (anti-)protons for central (0–5%) and peripheral (60–80%) Pb-Pb collisions at $\sqrt{s_{NN}} = 2.76$ TeV [28] and $\sqrt{s_{NN}} = 5.02$ TeV.

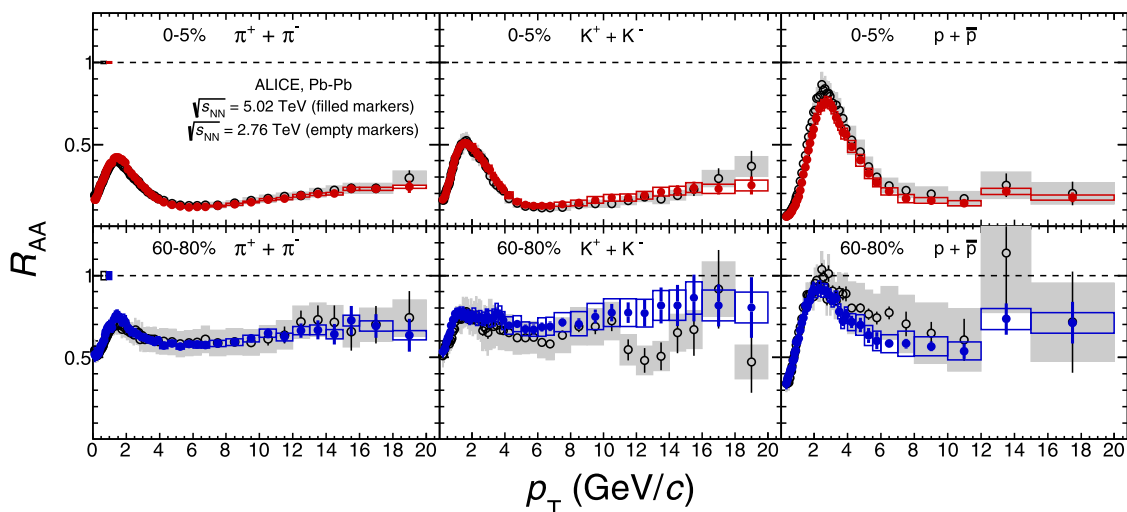


FIG. 10. Centrality dependence of the nuclear modification factor of charged π^\pm , K^\pm , and $(\bar{p})p$ as a function of transverse momentum, measured in Pb-Pb collisions at $\sqrt{s_{NN}} = 2.76$ [28] and 5.02 TeV, for 0–5% and 60–80% centrality classes. The statistical and systematic uncertainties are shown as error bars and boxes around the data points. The total normalization uncertainty (pp and Pb-Pb) is indicated in each panel by the vertical scale of the box centered at $p_T = 1$ GeV/c and $R_{AA} = 1$.

No significant dependence on the collision energy is observed, as also been observed for unidentified charged particles [95].

IV. COMPARISON TO MODELS

The results for identified particle production have been compared with the latest hydrodynamic model calculations based on the widely accepted “standard” picture of heavy-ion collisions [96]. These models all have similar ingredients: an initial state model provides the starting point for a viscous hydrodynamic calculation, chemical freeze-out occurs on a constant temperature hyper-surface, where local particle production is modeled with a statistical thermal model, and finally, the hadronic system is allowed to reinteract. The models used are: iEBE-VISHNU hybrid model [29,30], McGill [31], and EPOS [97]. In the following, specific features of each of them are described:

- (i) The iEBE-VISHNU model is an event-by-event version of the VISHNU hybrid model [98], which combines $(2 + 1) - d$ viscous hydrodynamics VISH2+1 [99,100] to describe the expansion of the sQGP fireball with a hadron cascade model (UrQMD) [101,102] to simulate the evolution of the system in the hadronic phase. The prediction of iEBE-VISHNU using either T_RENTo (Sec. III A) or a multiphase transport model (AMPT) [103] as initial conditions gives a good description of flow measurements in $\sqrt{s_{NN}} = 2.76$ TeV Pb-Pb collisions. T_RENTo parametrizes the initial entropy density via the reduced thickness function; AMPT constructs the initial energy density profiles using the energy decomposition of individual partons. Predictions by the iEBE-VISHNU hybrid model is available for p_T up to 3 GeV/c.
- (ii) The McGill model initial conditions rely on a new formulation of the IP-Glasma model [104], which

provides realistic event-by-event fluctuations and nonzero pre-equilibrium flow at the early stage of heavy-ion collisions. Individual collision systems are evolved using relativistic hydrodynamics with nonzero shear and bulk viscosities [105]. As the density of the system drops, fluid cells are converted into hadrons and further propagated microscopically using a hadronic cascade model [101,102]. The McGill predictions are available for p_T up to 4 GeV/c and centralities 0–60%.

- (iii) The EPOS model in the version EPOS3 is a phenomenological parton-based model that aims at modeling the full p_T range. EPOS is based on the theory of the Gribov-Regge multiple scattering, perturbative QCD, and string fragmentation [105]. However, dense regions in the system created in the collisions, the so-called core, is treated as a QGP and modeled with a hydrodynamic evolution followed by statistical hadronization. EPOS3 implements saturation in the initial state as predicted by the Color Glass Condensate model [106], a full viscous hydrodynamic simulation of the core, and a hadronic cascade, not present in the previous version of the model. EPOS3 implements also a new physics process that accounts for hydrodynamically expanding bulk matter, jets, and the interaction between the two, important for particle production at intermediate p_T [107] and reminiscent of the recombination mechanism [32,33].

Figure 11 shows the ratios of the p_T spectra in Pb-Pb collisions at $\sqrt{s_{NN}} = 5.02$ TeV to the models described above for $p_T < 4$ GeV/c. In the low p_T regime, one expects bulk particle production to dominate, so the absence of hard physics processes in the iEBE-VISHNU-T_RENTo, iEBE-VISHNU-AMPT, and McGill calculations is a minor issue. One observes that all models, in general, describe the spectra and the centrality dependence around $p_T \approx 1$ GeV/c within 20%. For $p_T < 3$ GeV/c the agreement with data is within 30%. The

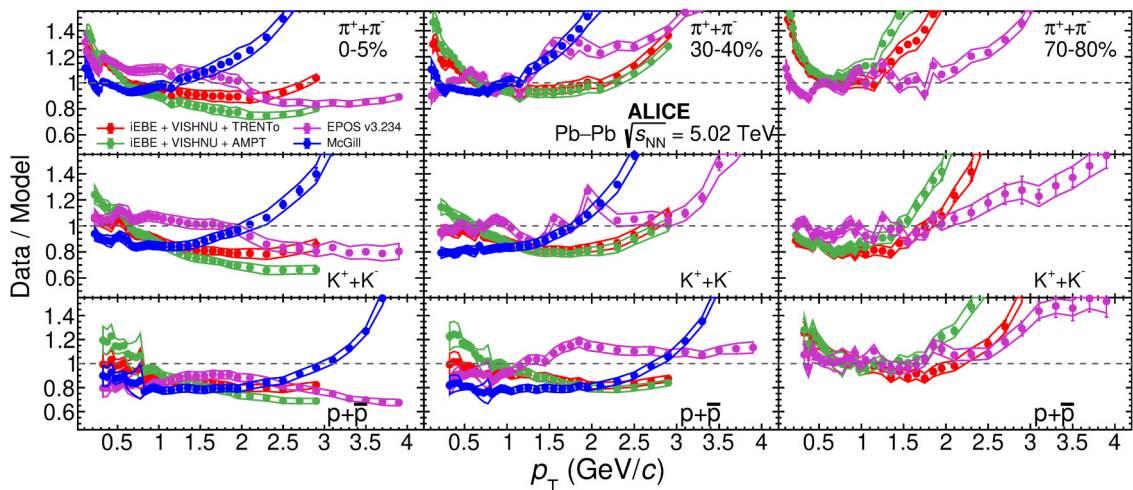


FIG. 11. Ratios of data to iEBE-VISHNU and McGill models (see text for details), for π^\pm , K^\pm and $(\bar{p})p$ p_T spectra in Pb-Pb collisions at $\sqrt{s_{NN}} = 5.02$ TeV for centrality classes 0-5%, 30-40% and 70-80%. The statistical and systematic uncertainties are shown as error bars and bands around the data points, respectively.

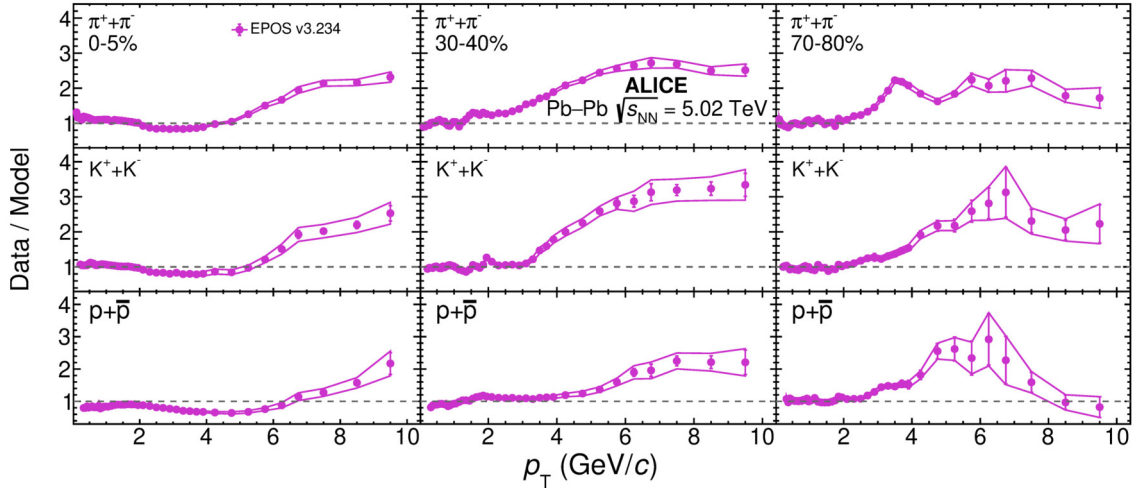


FIG. 12. Ratios of data to EPOS3 model (see text for details), for π^\pm , K^\pm , and $(\bar{p})p$ p_T spectra in Pb-Pb collisions at $\sqrt{s_{NN}} = 5.02$ TeV for centrality classes 0–5%, 30–40%, and 70–80%. The statistical and systematic uncertainties are shown as error bars and bands around the data points, respectively.

models agree with the proton (kaon) data over a broader p_T range than for kaons (pions). This mass hierarchy is expected from the hydrodynamic expansion, which introduces a mass dependence via the flow velocity – the larger the mass the larger the p_T boost. Similarly, it can be noticed that for the most central collisions the models describe the data over a broader p_T range than in peripheral ones. This is as expected from simple considerations. In central collisions, the system is larger and so the hydrodynamic expansion lasts longer, resulting in a stronger flow. At the same time, the fraction of the system involved in this expansion, the so-called core (e.g., the fraction of participant partons experiencing two or more binary collisions), is larger for the most central collisions. One can conclude that all four model calculations qualitatively describe the centrality dependence of radial flow and how

it is imprinted on the different particle species. Like the simplified blast-wave fits in Fig. 4, the two iEBE-VISHNU calculations also have difficulties to describe the very low p_T ($p_T < 0.5$ GeV/c) pion spectra.

Figure 12 shows the ratios of the p_T spectra in Pb-Pb collisions at $\sqrt{s_{NN}} = 5.02$ TeV to the EPOS3 model up to 10 GeV/c in p_T . EPOS3 includes both soft and hard physics processes, which should give a better description of data at high p_T and in peripheral collisions. However, its agreement with data is not significantly better than for the other models in the same p_T interval ($p_T < 3$ GeV/c) and at high p_T , it is about a factor 2 off with respect to data.

For completeness, Figs. 13, 14, and 15 show the comparison of the models with the p_T dependent particle ratios. The larger proton-to-pion ratio in EPOS3 than observed in the data

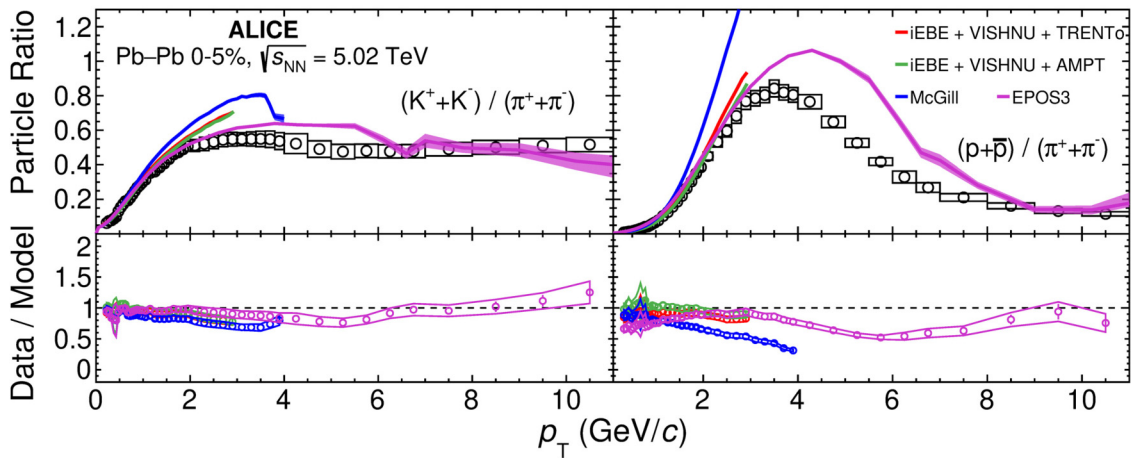


FIG. 13. (Top) K/π and p/π ratios in Pb-Pb collisions at $\sqrt{s_{NN}} = 5.02$ TeV in 0–5% centrality class, compared to iEBE-VISHNU, McGill, and EPOS3 model predictions; see text for details. The statistical and systematic uncertainties are shown as error bars and boxes around the data points, respectively. For model predictions the statistical uncertainties are represented by the band width. (Bottom) Data-to-model ratio, the statistical and systematic uncertainties are shown as error bars and bands around the data points, respectively.

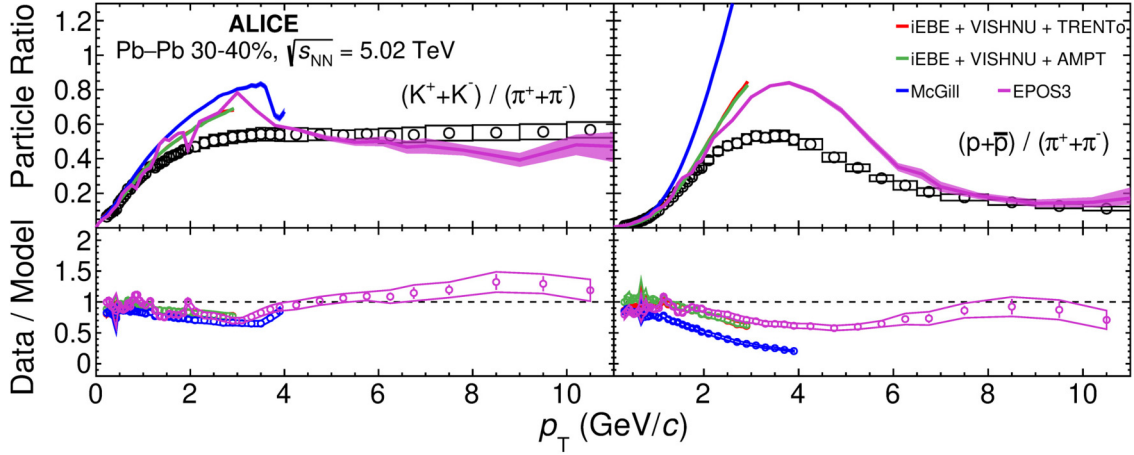


FIG. 14. (Top) K/π and p/π ratios in Pb-Pb collisions at $\sqrt{s_{NN}} = 5.02$ TeV in 30–40% centrality class, compared to iEBE-VISHNU, McGill, and EPOS3 model predictions; see text for details. The statistical and systematic uncertainties are shown as error bars and boxes around the data points, respectively. For model predictions the statistical uncertainties are represented by the band width. (Bottom) Data-to-model ratio, the statistical and systematic uncertainties are shown as error bars and bands around the data points, respectively.

can be understood as due to the underestimated pion yield in the model (see Fig. 12).

To compare the energy evolution of the spectra between data and model, in Fig. 16 is shown the ratio of the π^\pm , K^\pm , and $(\bar{p})p$ p_T spectra measured at $\sqrt{s_{NN}} = 5.02$ TeV to those measured at $\sqrt{s_{NN}} = 2.76$ TeV, compared to the same ratios obtained from model predictions.

For the McGill model, predictions at $\sqrt{s_{NN}} = 2.76$ TeV are currently not available. For central collisions, the agreement of the energy evolution in data and predictions is very good for both VISHNU initial-state models, while for peripheral collisions the AMPT initial conditions are better. For EPOS3 instead, a good agreement with data can be observed for both central and peripheral collisions. The comparison of model predictions to the ALICE measurements of anisotropic flow [108–110] can be useful to obtain tighter constraints on them.

V. CONCLUSIONS

In this paper, a comprehensive measurement of π^\pm , K^\pm and $(\bar{p})p$ production in inelastic pp and 0–90% central Pb-Pb collisions at $\sqrt{s_{NN}} = 5.02$ TeV at the LHC is presented. A clear evolution of the spectra with centrality is observed, with a power-law-like behavior at high p_T and a flattening of the spectra at low p_T , confirming previous results obtained in Pb-Pb collisions at $\sqrt{s_{NN}} = 2.76$ TeV. These features are compatible with the development of a strong collective flow with centrality, which dominates the spectral shapes up to relatively high p_T in central collisions. The p_T -integrated particle ratios as a function of $\langle dN_{ch}/d\eta \rangle$ in Pb-Pb at $\sqrt{s_{NN}} = 2.76$ and 5.02 TeV as well as in inelastic pp collisions at $\sqrt{s_{NN}} = 5.02$ TeV, have been compared. No significant energy dependence is observed, indicating that there is little or no dependence of the hadrochemistry

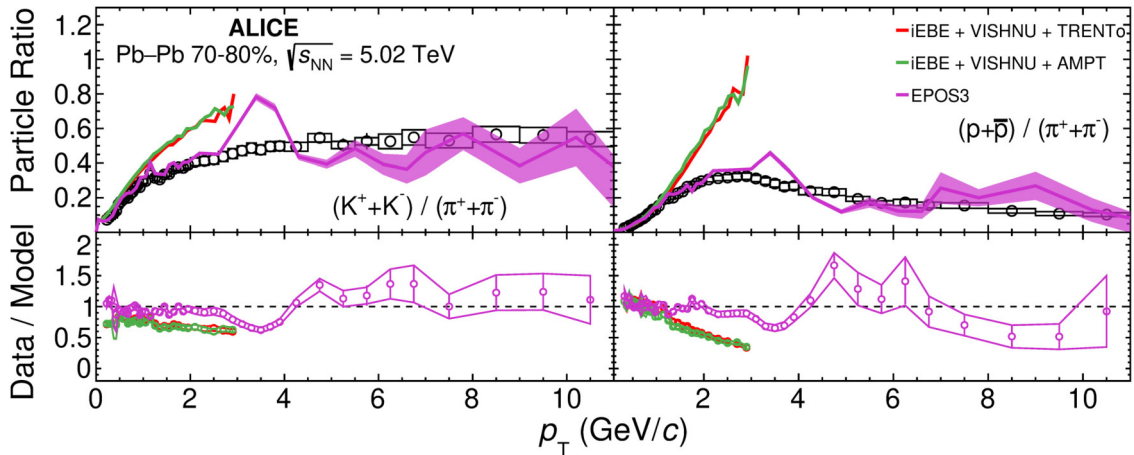


FIG. 15. (Top) K/π and p/π ratios in Pb-Pb collisions at $\sqrt{s_{NN}} = 5.02$ TeV in 70–80% centrality class, compared to iEBE-VISHNU, McGill, and EPOS3 model predictions; see text for details. The statistical and systematic uncertainties are shown as error bars and boxes around the data points, respectively. For model predictions the statistical uncertainties are represented by the band width. (Bottom) Data-to-model ratio, the statistical and systematic uncertainties are shown as error bars and bands around the data points, respectively.

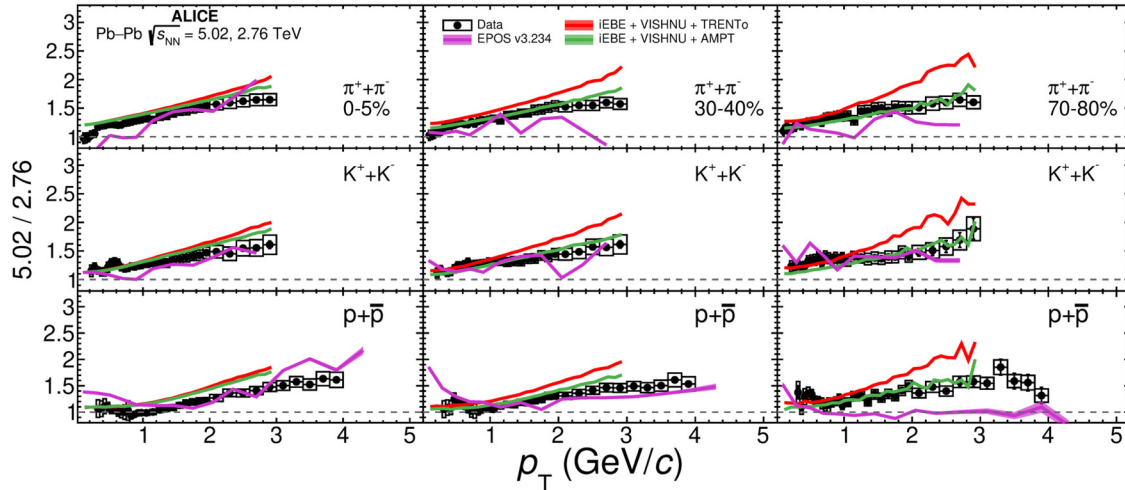


FIG. 16. π^\pm , K^\pm and $(\bar{p})p$ p_T spectra in Pb-Pb collisions at $\sqrt{s_{NN}} = 5.02$ TeV divided for the same spectra measured in Pb-Pb collisions at $\sqrt{s_{NN}} = 2.76$ TeV [28] for centrality classes 0–5%, 30–40%, and 70–80%, compared to iEBE-VISHNU, McGill, and EPOS3 model predictions; see text for details. The statistical and systematic uncertainties are shown as error bars and boxes around the data points, respectively. For model predictions the statistical uncertainties are represented by the band width.

on the collision energy. A blast-wave analysis of the p_T spectra gives an average transverse expansion velocity of $\langle\beta_T\rangle = 0.663 \pm 0.004$ in the most central (0–5%) Pb-Pb collisions that is $\approx 2\%$ larger than at $\sqrt{s_{NN}} = 2.76$ TeV, with a difference of ≈ 2.4 standard deviations between the two energies. The p_T -dependent particle ratios (p/π , K/π) show distinctive peaks at $p_T \approx 3$ GeV/ c in central Pb-Pb collisions, more pronounced for the proton-to-pion ratio. Such an increase with p_T is due to the mass ordering induced by the radial flow that would affect heavier particles more than lighter ones. The p_T of the peak position increases slightly with energy, in particular for the proton-to-pion ratio, indicating that the initially hotter system is longer lived so that radial flow is stronger. At high p_T , both particle ratios at $\sqrt{s_{NN}} = 5.02$ TeV are similar to those measured at $\sqrt{s_{NN}} = 2.76$ TeV and in pp collisions, suggesting that vacuumlike fragmentation processes dominate there. No significant evolution of nuclear modification at high- p_T with the center-of-mass energy is observed.

At high p_T , pions, kaons, and (anti-)protons are equally suppressed as observed at $\sqrt{s_{NN}} = 2.76$ TeV. This suggests that the large energy loss leading to the suppression is not associated with strong mass ordering or large fragmentation differences between baryons and mesons.

Transverse momentum spectra and particle ratios in Pb-Pb collisions are compared to different model calculations based on the standard QGP picture, which are found to describe the observed trends satisfactorily. For $p_T < 3$ GeV/ c , all models agree with the data within 30%, at $p_T \approx 1$ GeV/ c they describe the spectra and the centrality dependence within 20%.

ACKNOWLEDGMENTS

The ALICE Collaboration thanks all its engineers and technicians for their invaluable contributions to the construc-

tion of the experiment and the CERN accelerator teams for the outstanding performance of the LHC complex. The ALICE Collaboration gratefully acknowledges the resources and support provided by all Grid centres and the Worldwide LHC Computing Grid (WLCG) collaboration. The ALICE Collaboration acknowledges the following funding agencies for their support in building and running the ALICE detector: A. I. Alikhanyan National Science Laboratory (Yerevan Physics Institute) Foundation (ANSL), State Committee of Science and World Federation of Scientists (WFS), Armenia; Austrian Academy of Sciences, Austrian Science Fund (FWF) (Grant No. M 2467-N36) and Nationalstiftung für Forschung, Technologie und Entwicklung, Austria; Ministry of Communications and High Technologies, National Nuclear Research Center, Azerbaijan; Conselho Nacional de Desenvolvimento Científico e Tecnológico (CNPq), Financiadora de Estudos e Projetos (Finep), Fundação de Amparo à Pesquisa do Estado de São Paulo (FAPESP) and Universidade Federal do Rio Grande do Sul (UFRGS), Brazil; Ministry of Education of China (MOEC), Ministry of Science and Technology of China (MSTC) and National Natural Science Foundation of China (NSFC), China; Ministry of Science and Education and Croatian Science Foundation, Croatia; Centro de Aplicaciones Tecnológicas y Desarrollo Nuclear (CEADEN), Cubaenergía, Cuba; Ministry of Education, Youth and Sports of the Czech Republic, Czech Republic; The Danish Council for Independent Research | Natural Sciences, the VILLUM FONDEN and Danish National Research Foundation (DNRF), Denmark; Helsinki Institute of Physics (HIP), Finland; Commissariat à l’Energie Atomique (CEA), Institut National de Physique Nucléaire et de Physique des Particules (IN2P3) and Centre National de la Recherche Scientifique (CNRS) and Région des Pays de la Loire, France; Bundesministerium für Bildung und Forschung (BMBF) and GSI Helmholtzzentrum für Schwerionenforschung GmbH, Germany; General Secretariat for Research and Technology, Ministry of Education, Research

and Religions, Greece; National Research, Development and Innovation Office, Hungary; Department of Atomic Energy Government of India (DAE), Department of Science and Technology, Government of India (DST), University Grants Commission, Government of India (UGC) and Council of Scientific and Industrial Research (CSIR), India; Indonesian Institute of Science, Indonesia; Centro Fermi - Museo Storico della Fisica e Centro Studi e Ricerche Enrico Fermi and Istituto Nazionale di Fisica Nucleare (INFN), Italy; Institute for Innovative Science and Technology, Nagasaki Institute of Applied Science (IIST), Japanese Ministry of Education, Culture, Sports, Science and Technology (MEXT) and Japan Society for the Promotion of Science (JSPS) KAKENHI, Japan; Consejo Nacional de Ciencia (CONACYT) y Tecnología, through Fondo de Cooperación Internacional en Ciencia y Tecnología (FONCICYT) and Dirección General de Asuntos del Personal Académico (DGAPA), Mexico; Nederlandse Organisatie voor Wetenschappelijk Onderzoek (NWO), Netherlands; The Research Council of Norway, Norway; Commission on Science and Technology for Sustainable Development in the South (COMSATS), Pakistan; Pontificia Universidad Católica del Perú, Peru; Ministry of Science and Higher Education and National Science Centre, Poland; Korea Institute of Science and

Technology Information and National Research Foundation of Korea (NRF), Republic of Korea; Ministry of Education and Scientific Research, Institute of Atomic Physics and Ministry of Research and Innovation and Institute of Atomic Physics, Romania; Joint Institute for Nuclear Research (JINR), Ministry of Education and Science of the Russian Federation, National Research Centre Kurchatov Institute, Russian Science Foundation and Russian Foundation for Basic Research, Russia; Ministry of Education, Science, Research and Sport of the Slovak Republic, Slovakia; National Research Foundation of South Africa, South Africa; Swedish Research Council (VR) and Knut and Alice Wallenberg Foundation (KAW), Sweden; European Organization for Nuclear Research, Switzerland; Suranaree University of Technology (SUT), National Science and Technology Development Agency (NSDTA) and Office of the Higher Education Commission under NRU project of Thailand, Thailand; Turkish Atomic Energy Agency (TAEK), Turkey; National Academy of Sciences of Ukraine, Ukraine; Science and Technology Facilities Council (STFC), United Kingdom; National Science Foundation of the United States of America (NSF) and United States Department of Energy, Office of Nuclear Physics (DOE NP), United States of America.

-
- [1] I. Arsene *et al.* (BRAHMS Collaboration), Quark gluon plasma and color glass condensate at RHIC? The Perspective from the BRAHMS experiment, *Nucl. Phys. A* **757**, 1 (2005).
- [2] K. Adcox *et al.* (PHENIX Collaboration), Formation of dense partonic matter in relativistic nucleus-nucleus collisions at RHIC: Experimental evaluation by the PHENIX collaboration, *Nucl. Phys. A* **757**, 184 (2005).
- [3] B. B. Back *et al.*, The PHOBOS perspective on discoveries at RHIC, *Nucl. Phys. A* **757**, 28 (2005).
- [4] J. Adams *et al.* (STAR Collaboration), Experimental and theoretical challenges in the search for the quark gluon plasma: The STAR Collaboration's critical assessment of the evidence from RHIC collisions, *Nucl. Phys. A* **757**, 102 (2005).
- [5] J. Schukraft (ALICE Collaboration), Heavy ion physics with the ALICE experiment at the CERN LHC, *Philos. Trans. R. Soc. London A* **370**, 917 (2012).
- [6] U. Heinz and R. Snellings, Collective flow and viscosity in relativistic heavy-ion collisions, *Ann. Rev. Nucl. Part. Sci.* **63**, 123 (2013).
- [7] P. Braun-Munzinger, V. Koch, T. Schäfer, and J. Stachel, Properties of hot and dense matter from relativistic heavy ion collisions, *Phys. Rep.* **621**, 76 (2016).
- [8] L. Adamczyk *et al.* (STAR Collaboration), Bulk properties of the medium produced in relativistic heavy-ion collisions from the beam energy scan program, *Phys. Rev. C* **96**, 044904 (2017).
- [9] A. Andronic, P. Braun-Munzinger, K. Redlich, and J. Stachel, Decoding the phase structure of QCD via particle production at high energy, *Nature* **561**, 321 (2018).
- [10] F. Becattini, E. Grossi, M. Bleicher, J. Steinheimer, and R. Stock, Centrality dependence of hadronization and chemical freeze-out conditions in heavy ion collisions at $\sqrt{s_{NN}} = 2.76$ TeV, *Phys. Rev. C* **90**, 054907 (2014).
- [11] F. Becattini and L. Ferroni, Statistical hadronization and hadronic microcanonical ensemble 2, *Eur. Phys. J. C* **38**, 225 (2004); **66**, 341(E) (2010).
- [12] S. Acharya *et al.* (ALICE Collaboration), Production of ^4He and ^4He in Pb-Pb collisions at $\sqrt{s_{NN}} = 2.76$ TeV at the LHC, *Nucl. Phys. A* **971**, 1 (2018).
- [13] A. Bazavov *et al.* (HotQCD Collaboration), Equation of state in (2+1)-flavor QCD, *Phys. Rev. D* **90**, 094503 (2014).
- [14] B. Abelev *et al.* (ALICE Collaboration), Centrality dependence of π , K , p production in Pb-Pb collisions at $\sqrt{s_{NN}} = 2.76$ TeV, *Phys. Rev. C* **88**, 044910 (2013).
- [15] R. Stock, F. Becattini, M. Bleicher, T. Kollegger, T. Schuster, and J. Steinheimer, Hadronic freeze-out in $A + A$ collisions meets the lattice QCD Parton-Hadron transition line, *PoS (CPOD 2013)*, 011 (2013).
- [16] I. A. Karpenko, Yu. M. Sinyukov, and K. Werner, Uniform description of bulk observables in the hydrokinetic model of $A + A$ collisions at the BNL Relativistic Heavy Ion Collider and the CERN Large Hadron Collider, *Phys. Rev. C* **87**, 024914 (2013).
- [17] F. Becattini, M. Bleicher, T. Kollegger, T. Schuster, J. Steinheimer, and R. Stock, Hadron Formation in Relativistic Nuclear Collisions and the QCD Phase Diagram, *Phys. Rev. Lett.* **111**, 082302 (2013).
- [18] J. Steinheimer, J. Aichelin, and M. Bleicher, Nonthermal p/π Ratio at LHC as a Consequence of Hadronic Final State Interactions, *Phys. Rev. Lett.* **110**, 042501 (2013).
- [19] F. Becattini, J. Steinheimer, R. Stock, and M. Bleicher, Hadronization conditions in relativistic nuclear collisions and the QCD pseudocritical line, *Phys. Lett. B* **764**, 241 (2017).
- [20] S. Chatterjee, R. M. Godbole, and S. Gupta, Strange freezeout, *Phys. Lett. B* **727**, 554 (2013).

- [21] P. Alba, V. Vovchenko, M. I. Gorenstein, and H. Stoecker, Flavor-dependent eigenvolume interactions in a hadron resonance gas, *Nucl. Phys. A* **974**, 22 (2018).
- [22] P. Bozek and I. Wysłiel-Piekarska, Particle spectra in Pb-Pb collisions at $\sqrt{s_{NN}} = 2.76$ TeV, *Phys. Rev. C* **88**, 034907 (2012).
- [23] P. Bozek and I. Wysłiel-Piekarska, Particle spectra in Pb-Pb collisions at $\sqrt{s_{NN}} = 2.76$ TeV, *Phys. Rev. C* **85**, 064915 (2012).
- [24] R. J. Fries, B. Muller, C. Nonaka, and S. A. Bass, Hadron production in heavy ion collisions: Fragmentation and recombination from a dense parton phase, *Phys. Rev. C* **68**, 044902 (2003).
- [25] V. Topor Pop, M. Gyulassy, J. Barrette, C. Gale, X. N. Wang, and N. Xu, Baryon junction loops in HIJING/B anti-B v2.0 and the baryon/meson anomaly at RHIC, *Phys. Rev. C* **70**, 064906 (2004).
- [26] S. J. Brodsky and A. Sickles, The baryon anomaly: Evidence for color transparency and direct hadron production at RHIC, *Phys. Lett. B* **668**, 111 (2008).
- [27] B. B. Abelev *et al.* (ALICE Collaboration), K_S^0 and Λ Production in Pb-Pb Collisions at $\sqrt{s_{NN}} = 2.76$ TeV, *Phys. Rev. Lett.* **111**, 222301 (2013).
- [28] J. Adam *et al.* (ALICE Collaboration), Centrality dependence of the nuclear modification factor of charged pions, kaons, and protons in Pb-Pb collisions at $\sqrt{s_{NN}} = 2.76$ TeV, *Phys. Rev. C* **93**, 034913 (2016).
- [29] C. Shen, Z. Qiu, H. Song, J. Bernhard, S. Bass, and U. Heinz, The iEBE-VISHNU code package for relativistic heavy-ion collisions, *Comput. Phys. Commun.* **199**, 61 (2016).
- [30] W. Zhao, H.-j. Xu, and H. Song, Collective flow in 2.76 A TeV and 5.02 A TeV Pb+Pb collisions, *Eur. Phys. J. C* **77**, 645 (2017).
- [31] S. McDonald, C. Shen, F. Fillion-Gourdeau, S. Jeon, and C. Gale, Hydrodynamic predictions for Pb+Pb collisions at 5.02 TeV, *Phys. Rev. C* **95**, 064913 (2017).
- [32] V. Greco, C. M. Ko, and P. Levai, Parton Coalescence and Anti-Proton/Pion Anomaly at RHIC, *Phys. Rev. Lett.* **90**, 202302 (2003).
- [33] R. J. Fries, B. Muller, C. Nonaka, and S. A. Bass, Hadronization in Heavy Ion Collisions: Recombination and Fragmentation of Partons, *Phys. Rev. Lett.* **90**, 202303 (2003).
- [34] V. Minissale, F. Scardina, and V. Greco, Hadrons from coalescence plus fragmentation in AA collisions at energies available at the BNL Relativistic Heavy Ion Collider to the CERN Large Hadron Collider, *Phys. Rev. C* **92**, 054904 (2015).
- [35] B. B. Abelev *et al.* (ALICE Collaboration), Production of charged pions, kaons, and protons at large transverse momenta in pp and Pb-Pb collisions at $\sqrt{s_{NN}} = 2.76$ TeV, *Phys. Lett. B* **736**, 196 (2014).
- [36] K. M. Burke *et al.* (JET Collaboration), Extracting the jet transport coefficient from jet quenching in high-energy heavy-ion collisions, *Phys. Rev. C* **90**, 014909 (2014).
- [37] X.-N. Wang, What hard probes tell us about the quark-gluon plasma: Theory, *Nucl. Phys. A* **932**, 1 (2014).
- [38] B. Abelev *et al.* (ALICE Collaboration), Centrality determination of Pb-Pb collisions at $\sqrt{s_{NN}} = 2.76$ TeV with ALICE, *Phys. Rev. C* **88**, 044909 (2013).
- [39] C. Loizides, J. Kamin, and D. d'Enterria, Improved Monte Carlo Glauber predictions at present and future nuclear colliders, *Phys. Rev. C* **97**, 054910 (2018); **99**, 019901(E) (2019).
- [40] S. S. Adler *et al.* (PHENIX Collaboration), High p_T charged hadron suppression in Au + Au collisions at $\sqrt{s_{NN}} = 200$ GeV, *Phys. Rev. C* **69**, 034910 (2004).
- [41] J. Adams *et al.* (STAR Collaboration), Transverse Momentum and Collision Energy Dependence of High p_T Hadron Suppression in Au+Au Collisions at Ultrarelativistic Energies, *Phys. Rev. Lett.* **91**, 172302 (2003).
- [42] K. Aamodt *et al.* (ALICE Collaboration), Suppression of charged particle production at large transverse momentum in central Pb-Pb collisions at $\sqrt{s_{NN}} = 2.76$ TeV, *Phys. Lett. B* **696**, 30 (2011).
- [43] S. Chatrchyan *et al.* (CMS Collaboration), Study of high- p_T charged particle suppression in Pb-Pb compared to pp collisions at $\sqrt{s_{NN}} = 2.76$ TeV, *Eur. Phys. J. C* **72**, 1945 (2012).
- [44] G. Aad *et al.* (ATLAS Collaboration), Measurement of charged-particle spectra in Pb-Pb collisions at $\sqrt{s_{NN}} = 2.76$ TeV with the ATLAS detector at the LHC, *J. High Energy Phys.* **09** (2015) 050.
- [45] B. I. Abelev *et al.* (STAR Collaboration), Energy dependence of p^\pm , p , and anti- p transverse momentum spectra for Au+Au collisions at $\sqrt{s_{NN}} = 62.4$ and 200-GeV, *Phys. Lett. B* **655**, 104 (2007).
- [46] G. Agakishiev *et al.* (STAR Collaboration), Identified Hadron Compositions in $p + p$ and Au+Au Collisions at High Transverse Momenta at $\sqrt{s_{NN}} = 200$ GeV, *Phys. Rev. Lett.* **108**, 072302 (2012).
- [47] G.-Y. Qin and X.-N. Wang, Jet quenching in high-energy heavy-ion collisions, *Int. J. Mod. Phys. E* **24**, 1530014 (2015).
- [48] V. Khachatryan *et al.* (CMS Collaboration), Charged-particle nuclear modification factors in Pb – Pb and p – Pb collisions at $\sqrt{s_{NN}} = 5.02$ TeV, *J. High Energy Phys.* **04** (2017) 039.
- [49] V. Khachatryan *et al.* (CMS Collaboration), Measurement of inclusive jet cross sections in pp and PbPb collisions at $\sqrt{s_{NN}} = 2.76$ TeV, *Phys. Rev. C* **96**, 015202 (2017).
- [50] A. Adare *et al.* (PHENIX Collaboration), Scaling properties of fractional momentum loss of high- p_T hadrons in nucleus-nucleus collisions at $\sqrt{s_{NN}}$ from 62.4 GeV to 2.76 TeV, *Phys. Rev. C* **93**, 024911 (2016).
- [51] P. Christiansen, K. Tywoniuk, and V. Vislavicius, Universal scaling dependence of QCD energy loss from data-driven studies, *Phys. Rev. C* **89**, 034912 (2014).
- [52] A. Ortiz and O. Vázquez, Energy density and path-length dependence of the fractional momentum loss in heavy-ion collisions at $\sqrt{s_{NN}}$ from 62.4 to 5020 GeV, *Phys. Rev. C* **97**, 014910 (2018).
- [53] S. Acharya *et al.* (ALICE Collaboration), Transverse momentum spectra and nuclear modification factors of charged particles in Xe-Xe collisions at $\sqrt{s_{NN}} = 5.44$ TeV, *Phys. Lett. B* **788**, 166 (2019).
- [54] K. Aamodt *et al.* (ALICE Collaboration), The ALICE experiment at the CERN LHC, *J. Inst.* **3**, S08002 (2008).
- [55] B. B. Abelev *et al.* (ALICE Collaboration), Performance of the ALICE experiment at the CERN LHC, *Int. J. Mod. Phys. A* **29**, 1430044 (2014).
- [56] E. Abbas *et al.* (ALICE Collaboration), Performance of the ALICE VZERO system, *JINST* **8**, P10016 (2013).
- [57] K. Aamodt *et al.* (ALICE Collaboration), Alignment of the ALICE Inner Tracking System with cosmic-ray tracks, *JINST* **5**, P03003 (2010).

- [58] ALICE Collaboration, The ALICE definition of primary particles, <https://cds.cern.ch/record/2270008>.
- [59] J. Adam *et al.* (ALICE Collaboration), Measurement of pion, kaon and proton production in proton–proton collisions at $\sqrt{s} = 7$ TeV, *Eur. Phys. J. C* **75**, 226 (2015).
- [60] B. Abelev *et al.* (ALICE Collaboration), Pseudorapidity Density of Charged Particles in $p + \text{Pb}$ Collisions at $\sqrt{s_{NN}} = 5.02$ TeV, *Phys. Rev. Lett.* **110**, 032301 (2013).
- [61] J. Alme *et al.*, The ALICE TPC, a large three-dimensional tracking device with fast readout for ultra-high multiplicity events, *Nucl. Instrum. Meth. A* **622**, 316 (2010).
- [62] A. Akindinov *et al.*, Performance of the ALICE time-of-flight detector at the LHC, *Eur. Phys. J. Plus* **128**, 44 (2013).
- [63] P. Martinengo (ALICE Collaboration), The ALICE high momentum particle identification system: An overview after the first Large Hadron Collider run, *Nucl. Instrum. Meth. A* **639**, 7 (2011).
- [64] B. Abelev *et al.* (ALICE Collaboration), Pion, Kaon, and Proton Production in Central Pb-Pb Collisions at $\sqrt{s_{NN}} = 2.76$ TeV, *Phys. Rev. Lett.* **109**, 252301 (2012).
- [65] B. B. Abelev *et al.* (ALICE Collaboration), Multiplicity dependence of pion, kaon, proton and lambda production in p -Pb collisions at $\sqrt{s_{NN}} = 5.02$ TeV, *Phys. Lett. B* **728**, 25 (2014).
- [66] J. Adam *et al.* (ALICE Collaboration), Multiplicity dependence of charged pion, kaon, and (anti)proton production at large transverse momentum in p -Pb collisions at $\sqrt{s_{NN}} = 5.02$ TeV, *Phys. Lett. B* **760**, 720 (2016).
- [67] B. Abelev *et al.* (ALICE Collaboration), Technical design report for the upgrade of the ALICE inner tracking system, *J. Phys. G* **41**, 087002 (2014).
- [68] J. Adam *et al.* (ALICE Collaboration), Determination of the event collision time with the ALICE detector at the LHC, *Eur. Phys. J. Plus* **132**, 99 (2017).
- [69] D. Di Bari (ALICE Collaboration), The pattern recognition method for the CsI-RICH detector in ALICE, *Nucl. Instrum. Meth. A* **502**, 300 (2003).
- [70] P. Skands, S. Carrazza, and J. Rojo, Tuning PYTHIA 8.1: The Monash 2013 Tune, *Eur. Phys. J. C* **74**, 3024 (2014).
- [71] X.-N. Wang and M. Gyulassy, HIJING: A Monte Carlo model for multiple jet production in pp , pA , and AA collisions, *Phys. Rev. D* **44**, 3501 (1991).
- [72] R. Brun, F. Bruyant, M. Maire, A. C. McPherson, and P. Zancarini, GEANT 3: User's Guide Geant 3.10, Geant 3.11; rev. version (CERN, Geneva, 1987), <https://cds.cern.ch/record/1119728>.
- [73] S. Agostinelli *et al.* (GEANT4 Collaboration), GEANT4: A simulation toolkit, *Nucl. Instrum. Meth. A* **506**, 250 (2003).
- [74] K. Aamodt *et al.* (ALICE Collaboration), Midrapidity Antiproton-To-Proton Ratio in pp Collisions at $\sqrt{s} = 0.9$ and 7 TeV Measured by the ALICE Experiment, *Phys. Rev. Lett.* **105**, 072002 (2010).
- [75] G. Battistoni, S. Muraro, P. R. Sala, F. Cerutti, A. Ferrari, S. Roesler, A. Fasso, and J. Ranft, The FLUKA code: Description and benchmarking, *AIP Conf. Proc.* **896**, 31 (2007).
- [76] J. Adam *et al.* (ALICE Collaboration), Particle identification in ALICE: A Bayesian approach, *Eur. Phys. J. Plus* **131**, 168 (2016).
- [77] D. Cozza, D. Di Bari, A. Di Mauro, D. Elia, A. Morsch, E. Nappi, G. Paić, and F. Piuze, Recognition of Cherenkov patterns in high multiplicity environments, *Nucl. Instrum. Methods Phys. Res., Sect. A* **482**, 226 (2002).
- [78] S. Kretzer, Fragmentation functions from flavor inclusive and flavor tagged e^+e^- annihilations, *Phys. Rev. D* **62**, 054001 (2000).
- [79] E. Schnedermann, J. Sollfrank, and U. W. Heinz, Thermal phenomenology of hadrons from 200 AGeV S+S collisions, *Phys. Rev. C* **48**, 2462 (1993).
- [80] C. Tsallis, Possible generalization of Boltzmann-Gibbs statistics, *J. Statist. Phys.* **52**, 479 (1988).
- [81] B. I. Abelev *et al.* (STAR Collaboration), Strange particle production in $p + p$ collisions at $\sqrt{s} = 200$ GeV, *Phys. Rev. C* **75**, 064901 (2007).
- [82] U. W. Heinz, Concepts of heavy ion physics, in *Proceedings of the 2002 European School of High-Energy Physics, Pylos, Greece, 25 Aug–7 Sep 2002* (2004), pp. 165–238, <http://doc.cern.ch/yellowrep/CERN-2004-001>.
- [83] C. Loizides and A. Morsch, Absence of jet quenching in peripheral nucleus-nucleus collisions, *Phys. Lett. B* **773**, 408 (2017).
- [84] J. Adam *et al.* (ALICE Collaboration), Centrality dependence of the pseudorapidity density distribution for charged particles in Pb-Pb collisions at $\sqrt{s_{NN}} = 5.02$ TeV, *Phys. Lett. B* **772**, 567 (2017).
- [85] ALICE Collaboration, Centrality dependence of the charged-particle multiplicity density at midrapidity in Pb-Pb collisions at $\sqrt{s_{NN}} = 5.02$ TeV. <https://cds.cern.ch/record/2118084>.
- [86] J. Adam *et al.* (ALICE Collaboration), Enhanced production of multi-strange hadrons in high-multiplicity proton-proton collisions, *Nat. Phys.* **13**, 535 (2017).
- [87] A. Andronic, P. Braun-Munzinger, B. Friman, P. M. Lo, K. Redlich, and J. Stachel, The thermal proton yield anomaly in Pb-Pb collisions at the LHC and its resolution, *Phys. Lett. B* **792**, 304 (2019).
- [88] R. Stock, F. Becattini, M. Bleicher, and J. Steinheimer, The QCD phase diagram from statistical model analysis, *Nucl. Phys. A* **982**, 827 (2019).
- [89] J. E. Bernhard, J. S. Moreland, S. A. Bass, J. Liu, and U. Heinz, Applying Bayesian parameter estimation to relativistic heavy-ion collisions: Simultaneous characterization of the initial state and quark-gluon plasma medium, *Phys. Rev. C* **94**, 024907 (2016).
- [90] J. S. Moreland, J. E. Bernhard, and S. A. Bass, Alternative ansatz to wounded nucleon and binary collision scaling in high-energy nuclear collisions, *Phys. Rev. C* **92**, 011901 (2015).
- [91] A. Adare *et al.* (PHENIX Collaboration), Spectra and ratios of identified particles in Au+Au and d +Au collisions at $\sqrt{s_{NN}} = 200$ GeV, *Phys. Rev. C* **88**, 024906 (2013).
- [92] J. Adam *et al.* (ALICE Collaboration), $K^*(892)^0$ and $\phi(1020)$ meson production at high transverse momentum in pp and Pb-Pb collisions at $\sqrt{s_{NN}} = 2.76$ TeV, *Phys. Rev. C* **95**, 064606 (2017).
- [93] J. Adam *et al.* (ALICE Collaboration), Centrality dependence of particle production in p -Pb collisions at $\sqrt{s_{NN}} = 5.02$ TeV, *Phys. Rev. C* **91**, 064905 (2015).
- [94] S. Acharya *et al.* (ALICE Collaboration), Analysis of the apparent nuclear modification in peripheral Pb-Pb collisions at 5.02 TeV, *Phys. Lett. B* **793**, 420 (2019).
- [95] S. Acharya *et al.* (ALICE Collaboration), Transverse momentum spectra and nuclear modification factors of charged particles in pp , p -Pb, and Pb-Pb collisions at the LHC, *J. High Energy Phys.* **11** (2018) 013.

- [96] W. Busza, K. Rajagopal, and W. van der Schee, Heavy ion collisions: The big picture, and the big questions, *Ann. Rev. Nucl. Part. Sci.* **68**, 339 (2018).
- [97] K. Werner, B. Guiot, I. Karpenko, and T. Pierog, Analysing radial flow features in p -Pb and p - p collisions at several TeV by studying identified particle production in EPOS3, *Phys. Rev. C* **89**, 064903 (2014).
- [98] H. Song, S. A. Bass, and U. Heinz, Viscous QCD matter in a hybrid hydrodynamic+Boltzmann approach, *Phys. Rev. C* **83**, 024912 (2011).
- [99] H. Song and U. W. Heinz, Suppression of elliptic flow in a minimally viscous quark-gluon plasma, *Phys. Lett. B* **658**, 279 (2008).
- [100] H. Song and U. W. Heinz, Causal viscous hydrodynamics in 2+1 dimensions for relativistic heavy-ion collisions, *Phys. Rev. C* **77**, 064901 (2008).
- [101] M. Bleicher *et al.*, Relativistic hadron hadron collisions in the ultrarelativistic quantum molecular dynamics model, *J. Phys. G: Nucl. Part. Phys.* **25**, 1859 (1999).
- [102] S. A. Bass *et al.*, Microscopic models for ultrarelativistic heavy ion collisions, *Prog. Part. Nucl. Phys.* **41**, 255 (1998).
- [103] Z.-W. Lin, C. M. Ko, B.-A. Li, B. Zhang, and S. Pal, A Multi-phase transport model for relativistic heavy ion collisions, *Phys. Rev. C* **72**, 064901 (2005).
- [104] B. Schenke, P. Tribedy, and R. Venugopalan, Event-by-event gluon multiplicity, energy density, and eccentricities in ultrarelativistic heavy-ion collisions, *Phys. Rev. C* **86**, 034908 (2012).
- [105] S. Ryu, J. F. Paquet, C. Shen, G. S. Denicol, B. Schenke, S. Jeon, and C. Gale, Importance of the Bulk Viscosity of QCD in Ultrarelativistic Heavy-Ion Collisions, *Phys. Rev. Lett.* **115**, 132301 (2015).
- [106] F. Gelis, Color glass condensate and glasma, *Int. J. Mod. Phys. A* **28**, 1330001 (2013).
- [107] K. Werner, I. Karpenko, M. Bleicher, T. Pierog, and S. Porteboeuf-Houssais, Jets, bulk matter, and their interaction in heavy ion collisions at several TeV, *Phys. Rev. C* **85**, 064907 (2012).
- [108] S. Acharya *et al.* (ALICE Collaboration), Anisotropic flow of identified particles in Pb-Pb collisions at $\sqrt{s_{NN}} = 5.02$ TeV, *J. High Energy Phys.* **09** (2018) 006.
- [109] B. B. Abelev *et al.* (ALICE Collaboration), Elliptic flow of identified hadrons in Pb-Pb collisions at $\sqrt{s_{NN}} = 2.76$ TeV, *J. High Energy Phys.* **06** (2015) 190.
- [110] B. Abelev *et al.* (ALICE Collaboration), Anisotropic flow of charged hadrons, pions and (anti-)protons measured at high transverse momentum in Pb-Pb collisions at $\sqrt{s_{NN}} = 2.76$ TeV, *Phys. Lett. B* **719**, 18 (2013).

S. Acharya,¹⁴¹ D. Adamová,⁹³ S. P. Adhya,¹⁴¹ A. Adler,⁷³ J. Adolfsson,⁷⁹ M. M. Aggarwal,⁹⁸ G. Aglieri Rinella,³⁴ M. Agnello,³¹ N. Agrawal,^{10,48,53} Z. Ahammed,¹⁴¹ S. Ahmad,¹⁷ S. U. Ahn,⁷⁵ A. Akindinov,⁹⁰ M. Al-Turany,¹⁰⁵ S. N. Alam,¹⁴¹ D. S. D. Albuquerque,¹²² D. Aleksandrov,⁸⁶ B. Alessandro,⁵⁸ H. M. Alfanda,⁶ R. Alfaro Molina,⁷¹ B. Ali,¹⁷ Y. Ali,¹⁵ A. Alici,^{10,27,53} A. Alkin,² J. Alme,²² T. Alt,⁶⁸ L. Altenkamper,²² I. Altsybeev,¹¹² M. N. Anaam,⁶ C. Andrei,⁴⁷ D. Andreou,³⁴ H. A. Andrews,¹⁰⁹ A. Andronic,¹⁴⁴ M. Angeletti,³⁴ V. Anguelov,¹⁰² C. Anson,¹⁶ T. Antičić,¹⁰⁶ F. Antinori,⁵⁶ P. Antonioli,⁵³ R. Anwar,¹²⁵ N. Apadula,⁷⁸ L. Aphecetche,¹¹⁴ H. Appelshäuser,⁶⁸ S. Arcelli,²⁷ R. Arnaldi,⁵⁸ M. Arratia,⁷⁸ I. C. Arsene,²¹ M. Arslanovic,¹⁰² A. Augustinus,³⁴ R. Averbeck,¹⁰⁵ S. Aziz,⁶¹ M. D. Azmi,¹⁷ A. Badalà,⁵⁵ Y. W. Baek,⁴⁰ S. Bagnasco,⁵⁸ X. Bai,¹⁰⁵ R. Bailhache,⁶⁸ R. Bala,⁹⁹ A. Baldisseri,¹³⁷ M. Ball,⁴² S. Balouza,¹⁰³ R. C. Baral,⁸⁴ R. Barbera,²⁸ L. Barioglio,²⁶ G. G. Barnaföldi,¹⁴⁵ L. S. Barnby,⁹² V. Barret,¹³⁴ P. Bartalini,⁶ K. Barth,³⁴ E. Bartsch,⁶⁸ F. Baruffaldi,²⁹ N. Bastid,¹³⁴ S. Basu,¹⁴³ G. Batigne,¹¹⁴ B. Batyunya,⁷⁴ P. C. Batzing,²¹ D. Bauri,⁴⁸ J. L. Bazo Alba,¹¹⁰ I. G. Bearden,⁸⁷ C. Bedda,⁶³ N. K. Behera,⁶⁰ I. Belikov,¹³⁶ F. Bellini,³⁴ R. Bellwied,¹²⁵ V. Belyaev,⁹¹ G. Bencedi,¹⁴⁵ S. Beole,²⁶ A. Bercuci,⁴⁷ Y. Berdnikov,⁹⁶ D. Berenyi,¹⁴⁵ R. A. Bertens,¹³⁰ D. Berzano,⁵⁸ M. G. Besoiu,⁶⁷ L. Betev,³⁴ A. Bhasin,⁹⁹ I. R. Bhat,⁹⁹ M. A. Bhat,³ H. Bhatt,⁴⁸ B. Bhattacharjee,⁴¹ A. Bianchi,²⁶ L. Bianchi,²⁶ N. Bianchi,⁵¹ J. Bielčák,³⁷ J. Bielčková,⁹³ A. Bilandzic,^{103,117} G. Biro,¹⁴⁵ R. Biswas,³ S. Biswas,³ J. T. Blair,¹¹⁹ D. Blau,⁸⁶ C. Blume,⁶⁸ G. Boca,¹³⁹ F. Bock,³⁴ A. Bogdanov,⁹¹ L. Boldizsár,¹⁴⁵ A. Bolozdynya,⁹¹ M. Bombara,³⁸ G. Bonomi,¹⁴⁰ H. Borel,¹³⁷ A. Borissov,^{91,144} M. Borri,¹²⁷ H. Bossi,¹⁴⁶ E. Botta,²⁶ L. Bratrud,⁶⁸ P. Braun-Munzinger,¹⁰⁵ M. Bregant,¹²¹ T. A. Broker,⁶⁸ M. Broz,³⁷ E. J. Brucken,⁴³ E. Bruna,⁵⁸ G. E. Bruno,^{33,104} M. D. Buckland,¹²⁷ D. Budnikov,¹⁰⁷ H. Buesching,⁶⁸ S. Bufalino,³¹ O. Bugnon,¹¹⁴ P. Buhler,¹¹³ P. Buncic,³⁴ Z. Buthelezi,^{72,131} J. B. Butt,¹⁵ J. T. Buxton,⁹⁵ S. A. Bysiak,¹¹⁸ D. Caffarri,⁸⁸ A. Caliva,¹⁰⁵ E. Calvo Villar,¹¹⁰ R. S. Camacho,⁴⁴ P. Camerini,²⁵ A. A. Capon,¹¹³ F. Carnesecchi,^{10,27} R. Caron,¹³⁷ J. Castillo Castellanos,¹³⁷ A. J. Castro,¹³⁰ E. A. R. Casula,⁵⁴ F. Catalano,³¹ C. Ceballos Sanchez,⁵² P. Chakraborty,⁴⁸ S. Chandra,¹⁴¹ B. Chang,¹²⁶ W. Chang,⁶ S. Chapeland,³⁴ M. Chartier,¹²⁷ S. Chattopadhyay,¹⁴¹ S. Chattopadhyay,¹⁰⁸ A. Chauvin,²⁴ C. Cheshkov,¹³⁵ B. Cheynis,¹³⁵ V. Chibante Barroso,³⁴ D. D. Chinellato,¹²² S. Cho,⁶⁰ P. Chochula,³⁴ T. Chowdhury,¹³⁴ P. Christakoglou,⁸⁸ C. H. Christensen,⁸⁷ P. Christiansen,⁷⁹ T. Chujo,¹³³ C. Cicalo,⁵⁴ L. Cifarelli,^{10,27} F. Cindolo,⁵³ J. Cleymans,¹²⁴ F. Colamaria,⁵² D. Colella,⁵² A. Collu,⁷⁸ M. Colocci,²⁷ M. Concas,^{58,a} G. Conesa Balbastre,⁷⁷ Z. Conesa del Valle,⁶¹ G. Contin,^{59,127} J. G. Contreras,³⁷ T. M. Cormier,⁹⁴ Y. Corrales Morales,^{26,58} P. Cortese,³² M. R. Cosentino,¹²³ F. Costa,³⁴ S. Costanza,¹³⁹ P. Crochet,¹³⁴ E. Cuautle,⁶⁹ P. Cui,⁶ L. Cunqueiro,⁹⁴ D. Dabrowski,¹⁴² T. Dahms,^{103,117} A. Dainese,⁵⁶ F. P. A. Damas,^{114,137} M. C. Danisch,¹⁰² A. Danu,⁶⁷ D. Das,¹⁰⁸ I. Das,¹⁰⁸ P. Das,³ S. Das,³ A. Dash,⁸⁴ S. Dash,⁴⁸ A. Dashi,¹⁰³ S. De,^{49,84} A. De Caro,³⁰ G. de Cataldo,⁵² C. de Conti,¹²¹ J. de Cuveland,³⁹ A. De Falco,²⁴ D. De Gruttola,¹⁰ N. De Marco,⁵⁸ S. De Pasquale,³⁰ R. D. De Souza,¹²² S. Deb,⁴⁹ H. F. Degenhardt,¹²¹ K. R. Deja,¹⁴² A. Deloff,⁸³ S. Delsanto,^{26,131} D. Devetak,¹⁰⁵ P. Dhankher,⁴⁸ D. Di Bari,³³ A. Di Mauro,³⁴ R. A. Diaz,⁸ T. Dietel,¹²⁴ P. Dillenseger,⁶⁸ Y. Ding,⁶ R. Divià,³⁴ Ø. Djuvslund,²² U. Dmitrieva,⁶² A. Dobrin,^{34,67} B. Dönigus,⁶⁸ O. Dordic,²¹ A. K. Dubey,¹⁴¹ A. Dubla,¹⁰⁵ S. Dudi,⁹⁸ M. Dukhishyam,⁸⁴ P. Dupieux,¹³⁴ R. J. Ehlers,¹⁴⁶

- V. N. Eikeland,²² D. Elia,⁵² H. Engel,⁷³ E. Epple,¹⁴⁶ B. Erazmus,¹¹⁴ F. Erhardt,⁹⁷ A. Erokhin,¹¹² M. R. Ersdal,²² B. Espagnon,⁶¹ G. Eulisse,³⁴ J. Eum,¹⁸ D. Evans,¹⁰⁹ S. Evdokimov,⁸⁹ L. Fabbietti,^{103,117} M. Faggin,²⁹ J. Faivre,⁷⁷ F. Fan,⁶ A. Fantoni,⁵¹ M. Fasel,⁹⁴ P. Fedchio,³¹ A. Feliciello,⁵⁸ G. Feofilov,¹¹² A. Fernández Téllez,⁴⁴ A. Ferrero,¹³⁷ A. Ferretti,²⁶ A. Festanti,³⁴ V. J. G. Feuillard,¹⁰² J. Figiel,¹¹⁸ S. Filchagin,¹⁰⁷ D. Finogeev,⁶² F. M. Fionda,²² G. Fiorenza,⁵² F. Flor,¹²⁵ S. Foertsch,⁷² P. Foka,¹⁰⁵ S. Fokin,⁸⁶ E. Fragiaco,⁵⁹ U. Frankenfeld,¹⁰⁵ G. G. Fronze,²⁶ U. Fuchs,³⁴ C. Furget,⁷⁷ A. Furs,⁶² M. Fusco Girard,³⁰ J. J. Gaardhøje,⁸⁷ M. Gagliardi,²⁶ A. M. Gago,¹¹⁰ A. Gal,¹³⁶ C. D. Galvan,¹²⁰ P. Ganoti,⁸² C. Garabatos,¹⁰⁵ E. Garcia-Solis,¹¹ K. Garg,²⁸ C. Gargiulo,³⁴ A. Garibli,⁸⁵ K. Garner,¹⁴⁴ P. Gasik,^{103,117} E. F. Gauger,¹¹⁹ M. B. Gay Ducati,⁷⁰ M. Germain,¹¹⁴ J. Ghosh,¹⁰⁸ P. Ghosh,¹⁴¹ S. K. Ghosh,³ P. Gianotti,⁵¹ P. Giubellino,^{58,105} P. Giubilato,²⁹ P. Glässel,¹⁰² D. M. Gómez Coral,⁷¹ A. Gomez Ramirez,⁷³ V. Gonzalez,¹⁰⁵ P. González-Zamora,⁴⁴ S. Gorbunov,³⁹ L. Görlich,¹¹⁸ S. Gotovac,³⁵ V. Grabski,⁷¹ L. K. Graczykowski,¹⁴² K. L. Graham,¹⁰⁹ L. Greiner,⁷⁸ A. Grelli,⁶³ C. Grigoras,³⁴ V. Grigoriev,⁹¹ A. Grigoryan,¹ S. Grigoryan,⁷⁴ O. S. Groettkiv,²² F. Grosa,³¹ J. F. Grosse-Oetringhaus,³⁴ R. Grosso,¹⁰⁵ R. Guernane,⁷⁷ M. Guittiere,¹¹⁴ K. Gulbrandsen,⁸⁷ T. Gunji,¹³² A. Gupta,⁹⁹ R. Gupta,⁹⁹ I. B. Guzman,⁴⁴ R. Haake,¹⁴⁶ M. K. Habib,¹⁰⁵ C. Hadjidakis,⁶¹ H. Hamagaki,⁸⁰ G. Hamar,¹⁴⁵ M. Hamid,⁶ R. Hannigan,¹¹⁹ M. R. Haque,⁶³ A. Harlanderova,¹⁰⁵ J. W. Harris,¹⁴⁶ A. Harton,¹¹ J. A. Hasenbichler,³⁴ H. Hassan,⁷⁷ D. Hatzifotiadou,^{10,53} P. Hauer,⁴² S. Hayashi,¹³² A. D. L. B. Hechavarria,¹⁴⁴ S. T. Heckel,⁶⁸ E. Hellbär,⁶⁸ H. Helstrup,³⁶ A. Herghelegiu,⁴⁷ E. G. Hernandez,⁴⁴ G. Herrera Corral,⁹ F. Herrmann,¹⁴⁴ K. F. Hetland,³⁶ T. E. Hilden,⁴³ H. Hillemanns,³⁴ C. Hills,¹²⁷ B. Hippolyte,¹³⁶ B. Hohlweger,¹⁰³ D. Horak,³⁷ S. Hornung,¹⁰⁵ R. Hosokawa,^{16,133} P. Hristov,³⁴ C. Huang,⁶¹ C. Hughes,¹³⁰ P. Huhn,⁶⁸ T. J. Humanic,⁹⁵ H. Hushnud,¹⁰⁸ L. A. Husova,¹⁴⁴ N. Hussain,⁴¹ S. A. Hussain,¹⁵ D. Hutter,³⁹ D. S. Hwang,¹⁹ J. P. Iddon,^{34,127} R. Ilkaev,¹⁰⁷ M. Inaba,¹³³ M. Ippolitov,⁸⁶ M. S. Islam,¹⁰⁸ M. Ivanov,¹⁰⁵ V. Ivanov,⁹⁶ V. Izucheev,⁸⁹ B. Jacak,⁷⁸ N. Jacazio,^{27,53} P. M. Jacobs,⁷⁸ M. B. Jadhav,⁴⁸ S. Jadlovská,¹¹⁶ J. Jadlovsky,¹¹⁶ S. Jaelani,⁶³ C. Jahnke,¹²¹ M. J. Jakubowska,¹⁴² M. A. Janik,¹⁴² M. Jercic,⁹⁷ O. Jevons,¹⁰⁹ R. T. Jimenez Bustamante,¹⁰⁵ M. Jin,¹²⁵ F. Jonas,^{94,144} P. G. Jones,¹⁰⁹ J. Jung,⁶⁸ M. Jung,⁶⁸ A. Jusko,¹⁰⁹ P. Kalinak,⁶⁴ A. Kalweit,³⁴ J. H. Kang,¹⁴⁷ V. Kaplin,⁹¹ S. Kar,⁶ A. Karasu Uysal,⁷⁶ O. Karavichev,⁶² T. Karavicheva,⁶² P. Karczmarczyk,³⁴ E. Karpechev,⁶² U. Kobschull,⁷³ R. Keidel,⁴⁶ M. Keil,³⁴ B. Ketzer,⁴² Z. Khabanova,⁸⁸ A. M. Khan,⁶ S. Khan,¹⁷ S. A. Khan,¹⁴¹ A. Khanzadeev,⁹⁶ Y. Kharlov,⁸⁹ A. Khatun,¹⁷ A. Khuntia,¹¹⁸ B. Kileng,³⁶ B. Kim,⁶⁰ B. Kim,¹³³ D. Kim,¹⁴⁷ D. J. Kim,¹²⁶ E. J. Kim,¹³ H. Kim,¹⁴⁷ J. Kim,¹⁴⁷ J. S. Kim,⁴⁰ J. Kim,¹⁰² J. Kim,¹⁴⁷ J. Kim,¹³ M. Kim,¹⁰² S. Kim,¹⁹ T. Kim,¹⁴⁷ T. Kim,¹⁴⁷ S. Kirsch,³⁹ I. Kisel,³⁹ S. Kiselev,⁹⁰ A. Kisiel,¹⁴² J. L. Klay,⁵ C. Klein,⁶⁸ J. Klein,⁵⁸ S. Klein,⁷⁸ C. Klein-Bösing,¹⁴⁴ S. Klewin,¹⁰² A. Kluge,³⁴ M. L. Knichel,^{34,102} A. G. Knospe,¹²⁵ C. Kobdaj,¹¹⁵ M. K. Köhler,¹⁰² T. Kollegger,¹⁰⁵ A. Kondratyev,⁷⁴ N. Kondratyeva,⁹¹ E. Kondratyuk,⁸⁹ P. J. Konopka,³⁴ L. Koska,¹¹⁶ O. Kovalenko,⁸³ V. Kovalenko,¹¹² M. Kowalski,¹¹⁸ I. Králik,⁶⁴ A. Kravčáková,³⁸ L. Kreis,¹⁰⁵ M. Krivda,^{64,109} F. Krizek,⁹³ K. Krizkova Gajdosova,³⁷ M. Krüger,⁶⁸ E. Kryshen,⁹⁶ M. Krzewicki,³⁹ A. M. Kubera,⁹⁵ V. Kučera,⁶⁰ C. Kuhn,¹³⁶ P. G. Kuijper,⁸⁸ L. Kumar,⁹⁸ S. Kumar,⁴⁸ S. Kundu,⁸⁴ P. Kurashvili,⁸³ A. Kurepin,⁶² A. B. Kurepin,⁶² A. Kuryakin,¹⁰⁷ S. Kushpil,⁹³ J. Kvapil,¹⁰⁹ M. J. Kweon,⁶⁰ J. Y. Kwon,⁶⁰ Y. Kwon,¹⁴⁷ S. L. La Pointe,³⁹ P. La Rocca,²⁸ Y. S. Lai,⁷⁸ R. Langoy,¹²⁹ K. Lapidus,³⁴ A. Lardeux,²¹ P. Larionov,⁵¹ E. Laudi,³⁴ R. Lavicka,³⁷ T. Lazareva,¹¹² R. Lea,²⁵ L. Leardini,¹⁰² S. Lee,¹⁴⁷ F. Lehas,⁸⁸ S. Lehner,¹¹³ J. Lehrbach,³⁹ R. C. Lemmon,⁹² I. León Monzón,¹²⁰ E. D. Lesser,²⁰ M. Lettrich,³⁴ P. Lévai,¹⁴⁵ X. Li,¹² X. L. Li,⁶ J. Lien,¹²⁹ R. Lietava,¹⁰⁹ B. Lim,¹⁸ S. Lindal,²¹ V. Lindenstruth,³⁹ S. W. Lindsay,¹²⁷ C. Lippmann,¹⁰⁵ M. A. Lisa,⁹⁵ V. Litichevskiy,⁴³ A. Liu,⁷⁸ S. Liu,⁹⁵ W. J. Llope,¹⁴³ I. M. Lofnes,²² V. Loginov,⁹¹ C. Loizides,⁹⁴ P. Loncar,³⁵ X. Lopez,¹³⁴ E. López Torres,⁸ P. Luetig,⁶⁸ J. R. Lührer,¹⁴⁴ M. Lunardon,²⁹ G. Luparello,⁵⁹ A. Maevskaya,⁶² M. Mager,³⁴ S. M. Mahmood,²¹ T. Mahmoud,⁴² A. Maire,¹³⁶ R. D. Majka,¹⁴⁶ M. Malaev,⁹⁶ Q. W. Malik,²¹ L. Malinina,^{74,b} D. Mal'Kevich,⁹⁰ P. Malzacher,¹⁰⁵ G. Mandaglio,⁵⁵ V. Manko,⁸⁶ F. Manso,¹³⁴ V. Manzari,⁵² Y. Mao,⁶ M. Marchisone,¹³⁵ J. Mareš,⁶⁶ G. V. Margagliotti,²⁵ A. Margotti,⁵³ J. Margutti,⁶³ A. Marín,¹⁰⁵ C. Markert,¹¹⁹ M. Marquard,⁶⁸ N. A. Martin,¹⁰² P. Martinengo,³⁴ J. L. Martinez,¹²⁵ M. I. Martínez,⁴⁴ G. Martínez García,¹¹⁴ M. Martinez Pedreira,³⁴ S. Masciocchi,¹⁰⁵ M. Masera,²⁶ A. Masoni,⁵⁴ L. Massacrier,⁶¹ E. Masson,¹¹⁴ A. Mastroserio,^{52,138} A. M. Mathis,^{103,117} O. Matonoha,⁷⁹ P. F. T. Matuoka,¹²¹ A. Matyja,¹¹⁸ C. Mayer,¹¹⁸ M. Mazzilli,³³ M. A. Mazzoni,⁵⁷ A. F. Mechler,⁶⁸ F. Meddi,²³ Y. Melikyan,^{62,91} A. Menchaca-Rocha,⁷¹ C. Mengke,⁶ E. Meninno,³⁰ M. Meres,¹⁴ S. Mhlanga,¹²⁴ Y. Miake,¹³³ L. Micheletti,²⁶ D. L. Mihaylov,¹⁰³ K. Mikhaylov,^{74,90} A. Mischke,^{63,c} A. N. Mishra,⁶⁹ D. Miśkowiec,¹⁰⁵ C. M. Mitu,⁶⁷ A. Modak,³ N. Mohammadi,³⁴ A. P. Mohanty,⁶³ B. Mohanty,⁸⁴ M. Mohisin Khan,^{17,d} M. Mondal,¹⁴¹ C. Mordasini,¹⁰³ D. A. Moreira De Godoy,¹⁴⁴ L. A. P. Moreno,⁴⁴ S. Moretto,²⁹ A. Morreale,¹¹⁴ A. Morsch,³⁴ T. Mrnjavac,³⁴ V. Muccifora,⁵¹ E. Mudnic,³⁵ D. Mühlheim,¹⁴⁴ S. Muhuri,¹⁴¹ J. D. Mulligan,⁷⁸ M. G. Munhoz,¹²¹ K. Mürning,⁴² R. H. Munzer,⁶⁸ H. Murakami,¹³² S. Murray,¹²⁴ L. Musa,³⁴ J. Musinsky,⁶⁴ C. J. Myers,¹²⁵ J. W. Myrcha,¹⁴² B. Naik,⁴⁸ R. Nair,⁸³ B. K. Nandi,⁴⁸ R. Nania,^{10,53} E. Nappi,⁵² M. U. Naru,¹⁵ A. F. Nassirpour,⁷⁹ H. Natal da Luz,¹²¹ C. Nattrass,¹³⁰ R. Nayak,⁴⁸ T. K. Nayak,⁸⁴ S. Nazarenko,¹⁰⁷ A. Neagu,²¹ R. A. Negrão De Oliveira,⁶⁸ L. Nellen,⁶⁹ S. V. Nesbo,³⁶ G. Neskovic,³⁹ D. Nesterov,¹¹² B. S. Nielsen,⁸⁷ S. Nikolaev,⁸⁶ S. Nikulin,⁸⁶ V. Nikulin,⁹⁶ F. Noferini,^{10,53} P. Nomokonov,⁷⁴ G. Nooren,⁶³ J. Norman,⁷⁷ N. Novitzky,¹³³ P. Nowakowski,¹⁴² A. Nyanin,⁸⁶ J. Nystrand,²² M. Ogino,⁸⁰ A. Ohlson,¹⁰² J. Oleniacz,¹⁴² A. C. Oliveira Da Silva,¹²¹ M. H. Oliver,¹⁴⁶ C. Oppedisano,⁵⁸ R. Orava,⁴³ A. Ortiz Velasquez,⁶⁹ A. Oskarsson,⁷⁹ J. Otwinowski,¹¹⁸ K. Oyama,⁸⁰ Y. Pachmayer,¹⁰² V. Pacik,⁸⁷ D. Pagano,¹⁴⁰ G. Paić,⁶⁹ P. Palni,⁶ J. Pan,¹⁴³ A. K. Pandey,⁴⁸ S. Panebianco,¹³⁷ P. Pareek,⁴⁹ J. Park,⁶⁰ J. E. Parkkila,¹²⁶ S. Parmar,⁹⁸ S. P. Pathak,¹²⁵ R. N. Patra,¹⁴¹ B. Paul,^{24,58} H. Pei,⁶ T. Peitzmann,⁶³ X. Peng,⁶ L. G. Pereira,⁷⁰ H. Pereira Da Costa,¹³⁷ D. Peresunko,⁸⁶ G. M. Perez,⁸ E. Perez Lezama,⁶⁸ V. Peskov,⁶⁸ Y. Pestov,⁴ V. Petráček,³⁷ M. Petrovici,⁴⁷ R. P. Pezzi,⁷⁰ S. Piano,⁵⁹ M. Pikna,¹⁴ P. Pillot,¹¹⁴ L. O. D. L. Pimentel,⁸⁷ O. Pinazza,^{34,53} L. Pinsky,¹²⁵ C. Pinto,²⁸ S. Pisano,⁵¹ D. Pistone,⁵⁵ D. B. Piyarathna,¹²⁵ M. Płoskoń,⁷⁸ M. Planinic,⁹⁷

F. Pliquett,⁶⁸ J. Pluta,¹⁴² S. Pochybova,¹⁴⁵ M. G. Poghosyan,⁹⁴ B. Polichtchouk,⁸⁹ N. Poljak,⁹⁷ A. Pop,⁴⁷ H. Poppenborg,¹⁴⁴ S. Porteboeuf-Houssais,¹³⁴ V. Pozdniakov,⁷⁴ S. K. Prasad,³ R. Preghenella,⁵³ F. Prino,⁵⁸ C. A. Pruneau,¹⁴³ I. Pshenichnov,⁶² M. Puccio,^{26,34} V. Punin,¹⁰⁷ K. Puranapanda,¹⁴¹ J. Putschke,¹⁴³ R. E. Quishpe,¹²⁵ S. Ragoni,¹⁰⁹ S. Raha,³ S. Rajput,⁹⁹ J. Rak,¹²⁶ A. Rakotozafindrabe,¹³⁷ L. Ramello,³² F. Rami,¹³⁶ R. Raniwala,¹⁰⁰ S. S. Raniwala,¹⁰⁰ S. S. Räsänen,⁴³ B. T. Rascanu,⁶⁸ R. Rath,⁴⁹ V. Ratz,⁴² I. Ravasenga,³¹ K. F. Read,^{94,130} K. Redlich,^{83,e} A. Rehman,²² P. Reichelt,⁶⁸ F. Reidt,³⁴ X. Ren,⁶ R. Renfordt,⁶⁸ Z. Rescakova,³⁸ A. Reshetin,⁶² J.-P. Revol,¹⁰ K. Reygers,¹⁰² V. Riabov,⁹⁶ T. Richert,^{79,87} M. Richter,²¹ P. Riedler,³⁴ W. Riegler,³⁴ F. Riggi,²⁸ C. Ristea,⁶⁷ S. P. Rode,⁴⁹ M. Rodríguez Cahuantzi,⁴⁴ K. Røed,²¹ R. Rogalev,⁸⁹ E. Rogochaya,⁷⁴ D. Rohr,³⁴ D. Röhrich,²² P. S. Rokita,¹⁴² F. Ronchetti,⁵¹ E. D. Rosas,⁶⁹ K. Roslon,¹⁴² P. Rosnet,¹³⁴ A. Rossi,^{29,56} A. Rotondi,¹³⁹ F. Roukoutakis,⁸² A. Roy,⁴⁹ P. Roy,¹⁰⁸ O. V. Rueda,⁷⁹ R. Rui,²⁵ B. Romyantsev,⁷⁴ A. Rustamov,⁸⁵ E. Ryabinkin,⁸⁶ Y. Ryabov,⁹⁶ A. Rybicki,¹¹⁸ H. Rytönen,¹²⁶ S. Sadhu,¹⁴¹ S. Sadovsky,⁸⁹ K. Šafařík,^{34,37} S. K. Saha,¹⁴¹ B. Sahoo,⁴⁸ P. Sahoo,^{48,49} R. Sahoo,⁴⁹ S. Sahoo,⁶⁵ P. K. Sahu,⁶⁵ J. Saini,¹⁴¹ S. Sakai,¹³³ S. Sambyal,⁹⁹ V. Samsonov,^{91,96} A. Sandoval,⁷¹ A. Sarkar,⁷² D. Sarkar,¹⁴³ N. Sarkar,¹⁴¹ P. Sarma,⁴¹ V. M. Sarti,¹⁰³ M. H. P. Sas,⁶³ E. Scapparone,⁵³ B. Schaefer,⁹⁴ J. Schambach,¹¹⁹ H. S. Scheid,⁶⁸ C. Schiaua,⁴⁷ R. Schicker,¹⁰² A. Schmah,¹⁰² C. Schmidt,¹⁰⁵ H. R. Schmidt,¹⁰¹ M. O. Schmidt,¹⁰² M. Schmidt,¹⁰¹ N. V. Schmidt,^{68,94} A. R. Schmier,¹³⁰ J. Schukraft,^{34,87} Y. Schutz,^{34,136} K. Schwarz,¹⁰⁵ K. Schweda,¹⁰⁵ G. Scioli,²⁷ E. Scomparin,⁵⁸ M. Šefčík,³⁸ J. E. Seger,¹⁶ Y. Sekiguchi,¹³² D. Sekihata,^{45,132} I. Selyuzhenkov,^{91,105} S. Senyukov,¹³⁶ D. Serebryakov,⁶² E. Serradilla,⁷¹ P. Sett,⁴⁸ A. Sevcenco,⁶⁷ A. Shabanov,⁶² A. Shabetai,¹¹⁴ R. Shahoyan,³⁴ W. Shaikh,¹⁰⁸ A. Shangaraev,⁸⁹ A. Sharma,⁹⁸ A. Sharma,⁹⁹ H. Sharma,¹¹⁸ M. Sharma,⁹⁹ N. Sharma,⁹⁸ A. I. Sheikh,¹⁴¹ K. Shigaki,⁴⁵ M. Shimomura,⁸¹ S. Shirinkin,⁹⁰ Q. Shou,¹¹¹ Y. Sibiriak,⁸⁶ S. Siddhanta,⁵⁴ T. Siemiarczuk,⁸³ D. Silvermyr,⁷⁹ C. Silvestre,⁷⁷ G. Simatovic,⁸⁸ G. Simonetti,^{34,103} R. Singh,⁸⁴ R. Singh,⁹⁹ V. K. Singh,¹⁴¹ V. Singhal,¹⁴¹ T. Sinha,¹⁰⁸ B. Sitar,¹⁴ M. Sitta,³² T. B. Skaali,²¹ M. Slupecki,¹²⁶ N. Smirnov,¹⁴⁶ R. J. M. Snellings,⁶³ T. W. Snellman,^{43,126} J. Sochan,¹¹⁶ C. Soncco,¹¹⁰ J. Song,^{60,125} A. Songmoolnak,¹¹⁵ F. Soramel,²⁹ S. Sorensen,¹³⁰ I. Sputowska,¹¹⁸ M. Spyropoulou-Stassinaki,⁸² J. Stachel,¹⁰² I. Stan,⁶⁷ P. Stankus,⁹⁴ P. J. Steffanic,¹³⁰ E. Stenlund,⁷⁹ D. Stocco,¹¹⁴ M. M. Støretvedt,³⁶ L. D. Stritto,³⁰ P. Strmen,¹⁴ A. A. P. Suaide,¹²¹ T. Sugitate,⁴⁵ C. Suire,⁶¹ M. Suleymanov,¹⁵ M. Suljic,³⁴ R. Sultanov,⁹⁰ M. Šumbera,⁹³ S. Sumowidagdo,⁵⁰ S. Swain,⁶⁵ A. Szabo,¹⁴ I. Szarka,¹⁴ U. Tabassam,¹⁵ G. Taillepied,¹³⁴ J. Takahashi,¹²² G. J. Tambave,²² S. Tang,^{6,134} M. Tarhini,¹¹⁴ M. G. Tarzila,⁴⁷ A. Tauro,³⁴ G. Tejada Muñoz,⁴⁴ A. Telesca,³⁴ C. Terrevoli,^{29,125} D. Thakur,⁴⁹ S. Thakur,¹⁴¹ D. Thomas,¹¹⁹ F. Thoresen,⁸⁷ R. Tieulent,¹³⁵ A. Tikhonov,⁶² A. R. Timmins,¹²⁵ A. Toia,⁶⁸ N. Topilskaya,⁶² M. Toppi,⁵¹ F. Torales-Acosta,²⁰ S. R. Torres,¹²⁰ A. Trifiro,⁵⁵ S. Tripathy,⁴⁹ T. Tripathy,⁴⁸ S. Trogolo,²⁹ G. Trombetta,³³ L. Tropp,³⁸ V. Trubnikov,² W. H. Trzaska,¹²⁶ T. P. Trzcinski,¹⁴² B. A. Trzeciak,⁶³ T. Tsuji,¹³² A. Tumkin,¹⁰⁷ R. Turrisi,⁵⁶ T. S. Tveter,²¹ K. Ullaland,²² E. N. Umaka,¹²⁵ A. Uras,¹³⁵ G. L. Usai,²⁴ A. Utrobicic,⁹⁷ M. Vala,^{38,116} N. Valle,¹³⁹ S. Vallero,⁵⁸ N. van der Kolk,⁶³ L. V. R. van Doremalen,⁶³ M. van Leeuwen,⁶³ P. Vande Vyvre,³⁴ D. Varga,¹⁴⁵ Z. Varga,¹⁴⁵ M. Varga-Kofarago,¹⁴⁵ A. Vargas,⁴⁴ M. Vargyas,¹²⁶ R. Varma,⁴⁸ M. Vasileiou,⁸² A. Vasiliev,⁸⁶ O. Vázquez Doce,^{103,117} V. Vechernin,¹¹² A. M. Veen,⁶³ E. Vercellin,²⁶ S. Vergara Limón,⁴⁴ L. Vermunt,⁶³ R. Vernet,⁷ R. Vértesi,¹⁴⁵ M. G. D. L. C. Vicencio,⁹ L. Vickovic,³⁵ J. Viinikainen,¹²⁶ Z. Vilakazi,¹³¹ O. Villalobos Baillie,¹⁰⁹ A. Villatoro Tello,⁴⁴ G. Vino,⁵² A. Vinogradov,⁸⁶ T. Virgili,³⁰ V. Vislavicius,⁸⁷ A. Vodopyanov,⁷⁴ B. Volkel,³⁴ M. A. Völkl,¹⁰¹ K. Voloshin,⁹⁰ S. A. Voloshin,¹⁴³ G. Volpe,³³ B. von Haller,³⁴ I. Vorobyev,¹⁰³ D. Voscek,¹¹⁶ J. Vrláková,³⁸ B. Wagner,²² M. Weber,¹¹³ S. G. Weber,^{105,144} A. Wegrzynek,³⁴ D. F. Weiser,¹⁰² S. C. Wenzel,³⁴ J. P. Wessels,¹⁴⁴ J. Wiechula,⁶⁸ J. Wikne,²¹ G. Wilk,⁸³ J. Wilkinson,⁵³ G. A. Willems,³⁴ E. Willsher,¹⁰⁹ B. Windelband,¹⁰² W. E. Witt,¹³⁰ Y. Wu,¹²⁸ R. Xu,⁶ S. Yalcin,⁷⁶ K. Yamakawa,⁴⁵ S. Yang,²² S. Yano,¹³⁷ Z. Yin,⁶ H. Yokoyama,^{63,133} I.-K. Yoo,¹⁸ J. H. Yoon,⁶⁰ S. Yuan,²² A. Yuncu,¹⁰² V. Yurchenko,² V. Zaccolo,^{25,58} A. Zaman,¹⁵ C. Zampolli,³⁴ H. J. C. Zanoli,^{63,121} N. Zardoshti,³⁴ A. Zarochentsev,¹¹² P. Závada,⁶⁶ N. Zaviyalov,¹⁰⁷ H. Zbroszczyk,¹⁴² M. Zhalov,⁹⁶ X. Zhang,⁶ Z. Zhang,⁶ C. Zhao,²¹ V. Zherebchevskii,¹¹² N. Zhigareva,⁹⁰ D. Zhou,⁶ Y. Zhou,⁸⁷ Z. Zhou,²² J. Zhu,⁶ Y. Zhu,⁶ A. Zichichi,^{10,27} M. B. Zimmermann,³⁴ G. Zinovjev,² and N. Zurlo¹⁴⁰

(ALICE Collaboration)

¹A.I. Alikhanyan National Science Laboratory (Yerevan Physics Institute) Foundation, Yerevan, Armenia²Bogolyubov Institute for Theoretical Physics, National Academy of Sciences of Ukraine, Kiev, Ukraine³Bose Institute, Department of Physics and Centre for Astroparticle Physics and Space Science (CAPSS), Kolkata, India⁴Budker Institute for Nuclear Physics, Novosibirsk, Russia⁵California Polytechnic State University, San Luis Obispo, California, USA⁶Central China Normal University, Wuhan, China⁷Centre de Calcul de l'IN2P3, Villeurbanne, Lyon, France⁸Centro de Aplicaciones Tecnológicas y Desarrollo Nuclear (CEADEN), Havana, Cuba⁹Centro de Investigación y de Estudios Avanzados (CINVESTAV), Mexico City and Mérida, Mexico¹⁰Centro Fermi-Museo Storico della Fisica e Centro Studi e Ricerche "Enrico Fermi," Rome, Italy¹¹Chicago State University, Chicago, Illinois, USA¹²China Institute of Atomic Energy, Beijing, China¹³Chonbuk National University, Jeonju, Republic of Korea¹⁴Comenius University Bratislava, Faculty of Mathematics, Physics and Informatics, Bratislava, Slovakia

- ¹⁵COMSATS University Islamabad, Islamabad, Pakistan
¹⁶Creighton University, Omaha, Nebraska, USA
¹⁷Department of Physics, Aligarh Muslim University, Aligarh, India
¹⁸Department of Physics, Pusan National University, Pusan, Republic of Korea
¹⁹Department of Physics, Sejong University, Seoul, Republic of Korea
²⁰Department of Physics, University of California, Berkeley, California, USA
²¹Department of Physics, University of Oslo, Oslo, Norway
²²Department of Physics and Technology, University of Bergen, Bergen, Norway
²³Dipartimento di Fisica dell'Università 'La Sapienza' and Sezione INFN, Rome, Italy
²⁴Dipartimento di Fisica dell'Università and Sezione INFN, Cagliari, Italy
²⁵Dipartimento di Fisica dell'Università and Sezione INFN, Trieste, Italy
²⁶Dipartimento di Fisica dell'Università and Sezione INFN, Turin, Italy
²⁷Dipartimento di Fisica e Astronomia dell'Università and Sezione INFN, Bologna, Italy
²⁸Dipartimento di Fisica e Astronomia dell'Università and Sezione INFN, Catania, Italy
²⁹Dipartimento di Fisica e Astronomia dell'Università and Sezione INFN, Padova, Italy
³⁰Dipartimento di Fisica 'E.R. Caianiello' dell'Università and Gruppo Collegato INFN, Salerno, Italy
³¹Dipartimento DISAT del Politecnico and Sezione INFN, Turin, Italy
³²Dipartimento di Scienze e Innovazione Tecnologica dell'Università del Piemonte Orientale and INFN Sezione di Torino, Alessandria, Italy
³³Dipartimento Interateneo di Fisica 'M. Merlin' and Sezione INFN, Bari, Italy
³⁴European Organization for Nuclear Research (CERN), Geneva, Switzerland
³⁵Faculty of Electrical Engineering, Mechanical Engineering and Naval Architecture, University of Split, Split, Croatia
³⁶Faculty of Engineering and Science, Western Norway University of Applied Sciences, Bergen, Norway
³⁷Faculty of Nuclear Sciences and Physical Engineering, Czech Technical University in Prague, Prague, Czech Republic
³⁸Faculty of Science, P.J. Šafárik University, Košice, Slovakia
³⁹Frankfurt Institute for Advanced Studies, Johann Wolfgang Goethe-Universität Frankfurt, Frankfurt, Germany
⁴⁰Gangneung-Wonju National University, Gangneung, Republic of Korea
⁴¹Gauhati University, Department of Physics, Guwahati, India
⁴²Helmholtz-Institut für Strahlen- und Kernphysik, Rheinische Friedrich-Wilhelms-Universität Bonn, Bonn, Germany
⁴³Helsinki Institute of Physics (HIP), Helsinki, Finland
⁴⁴High Energy Physics Group, Universidad Autónoma de Puebla, Puebla, Mexico
⁴⁵Hiroshima University, Hiroshima, Japan
⁴⁶Hochschule Worms, Zentrum für Technologietransfer und Telekommunikation (ZTT), Worms, Germany
⁴⁷Horia Hulubei National Institute of Physics and Nuclear Engineering, Bucharest, Romania
⁴⁸Indian Institute of Technology Bombay (IIT), Mumbai, India
⁴⁹Indian Institute of Technology Indore, Indore, India
⁵⁰Indonesian Institute of Sciences, Jakarta, Indonesia
⁵¹INFN, Laboratori Nazionali di Frascati, Frascati, Italy
⁵²INFN, Sezione di Bari, Bari, Italy
⁵³INFN, Sezione di Bologna, Bologna, Italy
⁵⁴INFN, Sezione di Cagliari, Cagliari, Italy
⁵⁵INFN, Sezione di Catania, Catania, Italy
⁵⁶INFN, Sezione di Padova, Padova, Italy
⁵⁷INFN, Sezione di Roma, Rome, Italy
⁵⁸INFN, Sezione di Torino, Turin, Italy
⁵⁹INFN, Sezione di Trieste, Trieste, Italy
⁶⁰Inha University, Incheon, Republic of Korea
⁶¹Institut de Physique Nucléaire d'Orsay (IPNO), Institut National de Physique Nucléaire et de Physique des Particules (IN2P3/CNRS), Université de Paris-Sud, Université Paris-Saclay, Orsay, France
⁶²Institute for Nuclear Research, Academy of Sciences, Moscow, Russia
⁶³Institute for Subatomic Physics, Utrecht University/Nikhef, Utrecht, Netherlands
⁶⁴Institute of Experimental Physics, Slovak Academy of Sciences, Košice, Slovakia
⁶⁵Institute of Physics, Homi Bhabha National Institute, Bhubaneswar, India
⁶⁶Institute of Physics of the Czech Academy of Sciences, Prague, Czech Republic
⁶⁷Institute of Space Science (ISS), Bucharest, Romania
⁶⁸Institut für Kernphysik, Johann Wolfgang Goethe-Universität Frankfurt, Frankfurt, Germany
⁶⁹Instituto de Ciencias Nucleares, Universidad Nacional Autónoma de México, Mexico City, Mexico
⁷⁰Instituto de Física, Universidade Federal do Rio Grande do Sul (UFRGS), Porto Alegre, Brazil
⁷¹Instituto de Física, Universidad Nacional Autónoma de México, Mexico City, Mexico
⁷²iThemba LABS, National Research Foundation, Somerset West, South Africa

- ⁷³*Johann-Wolfgang-Goethe Universität Frankfurt Institut für Informatik, Fachbereich Informatik und Mathematik, Frankfurt, Germany*
- ⁷⁴*Joint Institute for Nuclear Research (JINR), Dubna, Russia*
- ⁷⁵*Korea Institute of Science and Technology Information, Daejeon, Republic of Korea*
- ⁷⁶*KTO Karatay University, Konya, Turkey*
- ⁷⁷*Laboratoire de Physique Subatomique et de Cosmologie, Université Grenoble-Alpes, CNRS-IN2P3, Grenoble, France*
- ⁷⁸*Lawrence Berkeley National Laboratory, Berkeley, California, USA*
- ⁷⁹*Lund University Department of Physics, Division of Particle Physics, Lund, Sweden*
- ⁸⁰*Nagasaki Institute of Applied Science, Nagasaki, Japan*
- ⁸¹*Nara Women's University (NWU), Nara, Japan*
- ⁸²*National and Kapodistrian University of Athens, School of Science, Department of Physics, Athens, Greece*
- ⁸³*National Centre for Nuclear Research, Warsaw, Poland*
- ⁸⁴*National Institute of Science Education and Research, Homi Bhabha National Institute, Jatni, India*
- ⁸⁵*National Nuclear Research Center, Baku, Azerbaijan*
- ⁸⁶*National Research Centre Kurchatov Institute, Moscow, Russia*
- ⁸⁷*Niels Bohr Institute, University of Copenhagen, Copenhagen, Denmark*
- ⁸⁸*Nikhef, National Institute for Subatomic Physics, Amsterdam, Netherlands*
- ⁸⁹*NRC Kurchatov Institute IHEP, Protvino, Russia*
- ⁹⁰*NRC Kurchatov Institute-ITEP, Moscow, Russia*
- ⁹¹*NRNU Moscow Engineering Physics Institute, Moscow, Russia*
- ⁹²*Nuclear Physics Group, STFC Daresbury Laboratory, Daresbury, United Kingdom*
- ⁹³*Nuclear Physics Institute of the Czech Academy of Sciences, Řež u Prahy, Czech Republic*
- ⁹⁴*Oak Ridge National Laboratory, Oak Ridge, Tennessee, USA*
- ⁹⁵*Ohio State University, Columbus, Ohio, USA*
- ⁹⁶*Petersburg Nuclear Physics Institute, Gatchina, Russia*
- ⁹⁷*Physics Department, Faculty of Science, University of Zagreb, Zagreb, Croatia*
- ⁹⁸*Physics Department, Panjab University, Chandigarh, India*
- ⁹⁹*Physics Department, University of Jammu, Jammu, India*
- ¹⁰⁰*Physics Department, University of Rajasthan, Jaipur, India*
- ¹⁰¹*Physikalisches Institut, Eberhard-Karls-Universität Tübingen, Tübingen, Germany*
- ¹⁰²*Physikalisches Institut, Ruprecht-Karls-Universität Heidelberg, Heidelberg, Germany*
- ¹⁰³*Physik Department, Technische Universität München, Munich, Germany*
- ¹⁰⁴*Politecnico di Bari, Bari, Italy*
- ¹⁰⁵*Research Division and ExtreMe Matter Institute EMMI, GSI Helmholtzzentrum für Schwerionenforschung GmbH, Darmstadt, Germany*
- ¹⁰⁶*Rudjer Bošković Institute, Zagreb, Croatia*
- ¹⁰⁷*Russian Federal Nuclear Center (VNIIEF), Sarov, Russia*
- ¹⁰⁸*Saha Institute of Nuclear Physics, Homi Bhabha National Institute, Kolkata, India*
- ¹⁰⁹*School of Physics and Astronomy, University of Birmingham, Birmingham, United Kingdom*
- ¹¹⁰*Sección Física, Departamento de Ciencias, Pontificia Universidad Católica del Perú, Lima, Peru*
- ¹¹¹*Shanghai Institute of Applied Physics, Shanghai, China*
- ¹¹²*St. Petersburg State University, St. Petersburg, Russia*
- ¹¹³*Stefan Meyer Institut für Subatomare Physik (SMI), Vienna, Austria*
- ¹¹⁴*SUBATECH, IMT Atlantique, Université de Nantes, CNRS-IN2P3, Nantes, France*
- ¹¹⁵*Suranaree University of Technology, Nakhon Ratchasima, Thailand*
- ¹¹⁶*Technical University of Košice, Košice, Slovakia*
- ¹¹⁷*Technische Universität München, Excellence Cluster 'Universe', Munich, Germany*
- ¹¹⁸*The Henryk Niewodniczanski Institute of Nuclear Physics, Polish Academy of Sciences, Cracow, Poland*
- ¹¹⁹*The University of Texas at Austin, Austin, Texas, USA*
- ¹²⁰*Universidad Autónoma de Sinaloa, Culiacán, Mexico*
- ¹²¹*Universidade de São Paulo (USP), São Paulo, Brazil*
- ¹²²*Universidade Estadual de Campinas (UNICAMP), Campinas, Brazil*
- ¹²³*Universidade Federal do ABC, Santo Andre, Brazil*
- ¹²⁴*University of Cape Town, Cape Town, South Africa*
- ¹²⁵*University of Houston, Houston, Texas, USA*
- ¹²⁶*University of Jyväskylä, Jyväskylä, Finland*
- ¹²⁷*University of Liverpool, Liverpool, United Kingdom*
- ¹²⁸*University of Science and Technology of China, Hefei, China*
- ¹²⁹*University of South-Eastern Norway, Tonsberg, Norway*
- ¹³⁰*University of Tennessee, Knoxville, Tennessee, USA*
- ¹³¹*University of the Witwatersrand, Johannesburg, South Africa*

¹³²*University of Tokyo, Tokyo, Japan*

¹³³*University of Tsukuba, Tsukuba, Japan*

¹³⁴*Université Clermont Auvergne, CNRS/IN2P3, LPC, Clermont-Ferrand, France*

¹³⁵*Université de Lyon, Université Lyon 1, CNRS/IN2P3, IPN-Lyon, Villeurbanne, Lyon, France*

¹³⁶*Université de Strasbourg, CNRS, IPHC UMR 7178, F-67000 Strasbourg, France, Strasbourg, France*

¹³⁷*Université Paris-Saclay Centre d'Etudes de Saclay (CEA), IRFU, Département de Physique Nucléaire (DPhN), Saclay, France*

¹³⁸*Università degli Studi di Foggia, Foggia, Italy*

¹³⁹*Università degli Studi di Pavia, Pavia, Italy*

¹⁴⁰*Università di Brescia, Brescia, Italy*

¹⁴¹*Variable Energy Cyclotron Centre, Homi Bhabha National Institute, Kolkata, India*

¹⁴²*Warsaw University of Technology, Warsaw, Poland*

¹⁴³*Wayne State University, Detroit, Michigan, USA*

¹⁴⁴*Westfälische Wilhelms-Universität Münster, Institut für Kernphysik, Münster, Germany*

¹⁴⁵*Wigner Research Centre for Physics, Hungarian Academy of Sciences, Budapest, Hungary*

¹⁴⁶*Yale University, New Haven, Connecticut, USA*

¹⁴⁷*Yonsei University, Seoul, Republic of Korea*

^aDipartimento DET del Politecnico di Torino, Turin, Italy.

^bM.V. Lomonosov Moscow State University, D.V. Skobeltsyn Institute of Nuclear Physics, Moscow, Russia.

^cDeceased.

^dDepartment of Applied Physics, Aligarh Muslim University, Aligarh, India.

^eInstitute of Theoretical Physics, University of Wrocław, Poland.